Potential of Ka-Band Range Rate Post-Fit Residuals for High-Frequency Mass Change Applications

Cuadrat-Grzybowski, M.; Encarnacao, J. G. Teixeira da; Visser, P. N. A. M.

DOI
10.1029/2025JB031615

Publication date
2025

Document Version
Final published version

Published in
Journal of Geophysical Research: Solid Earth

Citation (APA)
Cuadrat-Grzybowski, M., Encarnacao, J. G. T. D., & Visser, P. N. A. M. (2025). Potential of Ka-Band Range Rate Post-Fit Residuals for High-Frequency Mass Change Applications. *Journal of Geophysical Research: Solid Earth*, *130*(12), Article e2025JB031615. https://doi.org/10.1029/2025JB031615

JGR Solid Earth

RESEARCH ARTICLE
10.1029/2025JB031615

Potential of Ka-Band Range Rate Post-Fit Residuals for High-Frequency Mass Change Applications

M. Cuadrat-Grzybowski[1], **J. G. Teixeira da Encarnacao**[1], **and P. N. A. M. Visser**[1]

[1]Astrodynamics and Space Missions section, Space Engineering, Delft University of Technology, HS Delft, The Netherlands

Abstract We present the first extensive analysis of K/Ka-band ranging post-fit residuals of an official Level-2 product, characterized as Line-of-Sight Gravity Differences (LGD), which exhibit and showcase interesting sub-monthly geophysical signals. These residuals, provided by Center for Space Research, were derived from the difference between spherical harmonic coefficient least-squares fits and reduced Level-1B range-rate observations. We classified the geophysical signals into four distinct categories: oceanic, meteorological, hydrological, and solid Earth, focusing primarily on the first three categories in this study. In our examination of oceanic processes, we identified notable mass anomalies in the Argentine basin, specifically within the Zapiola Rise, where persistent remnants of the rotating dipole-like modes are evident in the LGD post-fit residuals. Our analysis extended to the Gulf of Carpentaria and Australia during the 2013 Oswald cyclone, revealing significant LGD residual anomalies that correlate with cyclone tracking and precipitation data. Additionally, we investigated the monsoon seasons in Bangladesh, particularly from June–September 2007, where we observed peaks in sub-monthly variability. These findings were further validated by demonstrating high spatial and temporal correlations between gridded LGD residuals and ITSG-Grace2018 daily solutions. These identified anomalies are associated with significant mass change phenomena, underscoring the critical importance of these geophysical signals for future high-resolution studies of mass transport.

Plain Language Summary Understanding changes in Earth's gravity is important for monitoring environmental events. For this purpose, researchers have traditionally used monthly averaged data from the Gravity Recovery and Climate Experiment (GRACE) and GRACE-FO satellites. While monthly models are effective for tracking long-term trends and seasonal changes, they often miss rapid events, such as sudden floods, and fast changes in pressure and circulation. In our study, we explored an alternative approach by utilizing Level-1B data from the GRACE satellites, which are inputs used to generate these monthly models. We focused on ("post-fit") residual data, which highlights differences between the satellite observations and the best orbital predictions. We identified quick mass changes in the oceans and land that the traditional method overlooked. For instance, we detected rapid changes in the Argentine (ocean) basin. We also saw the effects of the Oswald cyclone in January 2013, in Australia. Lastly, we analyzed the major 2007 monsoon floods in Bangladesh and validated our results using alternative daily gravity data. We were able to show the location of these flooding events with better accuracy. This type of analysis could greatly enhance our ability to monitor and respond to fast-changing events, improving our understanding and management of natural disasters.

Key Points:

- *K*-Band Ranging post-fit residuals from monthly Level-2 processing contain substantial submonthly mass change geophysical signals
- Post-fit residuals, expressed in the Line-of-Sight Gravity Difference form, are used to identify and characterize geophysical signals
- Submonthly geophysical signals in post-fit residuals show high correlations with ITSG-Grace2018 daily solutions, validating their detection

Supporting Information:

Supporting Information may be found in the online version of this article.

Correspondence to:

M. Cuadrat-Grzybowski,
M.Cuadrat-Grzybowski-1@tudelft.nl

Citation:

Cuadrat-Grzybowski, M., Teixeira da Encarnacao, J. G., & Visser, P. N. A. M. (2025). Potential of Ka-band range rate post-fit residuals for high-frequency mass change applications. *Journal of Geophysical Research: Solid Earth*, *130*, e2025JB031615. https://doi.org/10.1029/2025JB031615

Received 20 MAR 2025
Accepted 26 NOV 2025

Author Contributions:

Conceptualization: M. Cuadrat-Grzybowski, J. G. Teixeira da Encarnacao, P. N. A. M. Visser
Data curation: M. Cuadrat-Grzybowski, J. G. Teixeira da Encarnacao
Formal analysis: M. Cuadrat-Grzybowski, J. G. Teixeira da Encarnacao, P. N. A. M. Visser
Investigation: M. Cuadrat-Grzybowski, J. G. Teixeira da Encarnacao
Methodology: M. Cuadrat-Grzybowski, J. G. Teixeira da Encarnacao
Software: M. Cuadrat-Grzybowski
Supervision: J. G. Teixeira da Encarnacao, P. N. A. M. Visser
Validation: M. Cuadrat-Grzybowski

1. Introduction

The Gravity Recovery and Climate Experiment (GRACE) and its follow-on (FO) mission, GRACE-FO, have revolutionized our understanding of Earth's gravity field and mass redistribution. These missions provide monthly solutions of spherical harmonic (SH) and mascon (mass concentrations)-based models, which have been widely utilized in hydrology, glaciology, oceanography, and solid Earth dynamics studies (Schmidt et al., 2008; Wahr, 2015; Wouters et al., 2019; Xiong et al., 2024). The primary data products from GRACE are made available by the GRACE Science Data System, composed of the Center for Space Research (CSR), the Jet Propulsion Laboratory (JPL), and GeoForschungsZentrum Potsdam (GFZ), which generate monthly SH models (also known as Level-2 or L2) through the Least-Squares fitting of reduced Level-1B (L1B) observations, resulting in a set of L2 SH or/and mascon-related coefficients (part of the Level-3 data).

Research efforts aimed at improving the temporal resolution of GRACE (-FO) solutions led to the development of 10-day (Lemoine & Bourgogne, 2020), weekly (Flechtner et al., 2010), and even daily (Kurtenbach et al., 2012)

Visualization: M. Cuadrat-Grzybowski
Writing – original draft: M. Cuadrat-Grzybowski
Writing – review & editing: M. Cuadrat-Grzybowski, J. G. Teixeira da Encarnacao, P. N. A. M. Visser

SH and mascon products (Bonin & Save, 2020; Croteau et al., 2020). Currently, daily solutions produced using Kalman filtering techniques, such as the ITSG-Grace2018 solutions (Kurtenbach et al., 2012; Mayer-Gürr et al., 2018) and other studies (Kvas et al., 2019; Ramillien et al., 2020), represent the state-of-the-art in terms of temporal resolution. Even though GRACE daily ground coverage (of 15 revolutions) is not sufficient for global gravity recovery, these daily solutions were stabilized by applying a backward and forward Kalman smoother on daily GRACE data with the addition of de-aliasing sub-monthly hydrological background models (Kvas et al., 2019). Gouweleeuw et al. (2018) were the first to use ITSG-Grace2014 daily solutions to demonstrate that GRACE could observe sub-monthly hydrological signals related to severe flooding events during Bangladesh's monsoon seasons. Furthermore, daily solutions were used to constrain high-frequency hydro-meteorological flux models over continents for the first time (Eicker et al., 2020). However as previously mentioned, other than GRACE (-FO) data, these daily models require the assimilation of additional (hydrological) information for stability. CSR developed GRACE-only daily swaths (limited at ±66 deg latitude) for high-frequency oceanographic applications, which were able to explain 25%–75% sub-monthly altimetry-based observations of mass change (Bonin & Save, 2020; Schindelegger et al., 2021). Furthermore, CSR is currently developing 5-day (5D) solutions, which showed promising results for flood monitoring and forecasting, with hydrological traces from the 2005 Katrina hurricane identified (Rateb et al., 2024; Sun et al., 2024). However, increasing temporal resolution inherently leads to a reduction of spatial resolution, leading to a trade-off between the two. This trade-off sparked interest in alternative approaches that bypassed the SH and mascon frameworks.

One method involves analyzing Level-1B data directly, and not the resulting SH or mascon solutions. By working with along-orbit observations, with 5s-sampling, researchers have the potential to directly observe mass variations sensed by GRACE. This approach, when combined with corrections for background models, accelerometer scale and bias factors, and initial state vector inaccuracies, could offer the highest spatial and temporal resolutions. Ghobadi-Far et al. (2019) derived analytical expressions that relate gravimetric observables (such as gravity disturbance potential and gravity gradients) from residual L1B data (i.e., range rate and range acceleration). Allgeyer et al. (2022) demonstrated the benefit of using time-filtered pre-fit range accelerations when deriving mascon models via regularization, which incorporated model covariance constraints and mass conservation. To effectively eliminate the centrifugal acceleration in L1B range acceleration data, Ghobadi-Far et al. (2018) derived an analytical frequency-based transfer function from range acceleration to Line-of-Sight Gravity (LGD), which better localizes mass anomalies on the Earth's surface. Using both range acceleration and LGDs has been particularly valuable in detecting high-frequency mass change events, which have included events such as tsunamis, earthquakes, cyclones, and extreme hydrological events like floods and droughts, as highlighted by recent studies (Ghobadi-Far et al., 2020, 2022; Peidou et al., 2022). Additionally, Han, Yeo et al. (2021) used residual L1B LGDs to estimate rapid changes in water storage due to heavy rainfall and flooding in Australia in March 2021, following extreme drought events in 2019–2020. In the context of solid Earth applications, Han et al. (2010) first showed the range rate signature in L1B data related to the 2010 Maule earthquake and later Ghobadi-Far et al. (2020) demonstrated that residual L1B data in the form of LGDs can also localize the loading effects of tsunamis after major earthquake events such as Sumatra 2004 and Tohoku 2011. Lastly, Peidou et al. (2022) performed an entire spatial and temporal characterization of GRACE data in terms of range accelerations, which showed that post-fit residuals (obtained after the monthly Least Squares gravity inversion) show sub-monthly geophysical signal. All these studies emphasize the presence of sub-monthly signals within the GRACE L1B data, revealing high-frequency mass change processes by avoiding the SH/mascon monthly representation.

In this study, we consider RL06 CSR L1B post-fit residuals (from the GRACE era only), which are the difference between the pre-fits and the least-squares SH fit, along with additional corrections for "common" and "local" parameters, which is a terminology used by, for example, (Pini, 2012). The pre-fits are the difference between the (preprocessed) K/Ka-Band Ranging (KBR) measurements and predicted inter-satellite distance generated on the basis of a comprehensive background force model. As these post-fit residuals represent the errors of a widely used L2 product, the research question that this study answers is

> *How can high-frequency geophysical signals within GRACE Level-1B post-fit residuals be identified, characterized, and validated using spatial correlation analysis and comparisons with daily gravity field solutions?*

We characterize and analyze the high-frequency signals in post-fit residuals to gain insights into sub-monthly mass change phenomena. These residuals reveal important information that the monthly SH coefficients

cannot explain, in addition to unmodelled effects from background models and accelerometer calibration parameters (Peidou et al., 2022). The novelty of this study lies in the in-depth spatial and temporal analysis of sub-monthly signals in CSR's L1B post-fit residuals, offering a more detailed exploration of geophysical phenomena compared to previous studies (Ghobadi-Far et al., 2022; Peidou et al., 2022), and the characterization of error of an official L2 data product. We also show the high resolution with which GRACE can effectively resolve and differentiate various geophysical categories of sub-monthly variations in Earth's time-variable gravity field.

The paper is organized as follows: Section 2 describes the data utilized in the study, while Section 3 outlines the methodology employed for analyzing high-frequency signals. Section 4 focuses on the analysis of KBR residual L1B data in the context of sub-monthly mass change variations, and Section 5 presents the conclusions.

2. Data

2.1. Residual Level-1B Data

In this study, we use an intermediate GRACE product between Level-1B and Level-2, provided by CSR, denoted here as the residual Level-1B data product. GRACE Level-1B data are derived from the Level-1A data, which are the processed telemetry measurements converted to engineering units obtained from the satellites' instruments. The Level-1A data undergo extensive and irreversible preprocessing, resulting in Level-1B data products, available at 1–5 s sampling rates.

The residual Level-1B data used in this study consist of CSR's RL06 residual KBR Level-1B data for the entire duration of the GRACE mission, which spanned from April 2002 to June 2017. We received both the residual Level-1B data (known as *pre-fit*) and the corresponding Least-Squares fit after the gravity retrieval, limited to degree 180. The post-fit data can be found in https://doi.org/10.18738/T8/VY3U8L (S. Bettadpur et al., 2025), whereas the original Level-1B data sets, generated by the JPL, can be accessed publicly (Case et al., 2010a) at https://doi.org/10.5067/GRJPL-L1B03. Additionally, the processing standards and details developed by CSR (S. V. Bettadpur, 2018) to transition from Level-1B to Level-2 are also available to the public.

In this context, we define the following three essential variables associated with the range-rate processing:

- *Pre-fit* $\left(\delta\dot{\rho}\right)$: Represents the reduced Level-1B K-band range-rate observations, obtained after subtracting background models (e.g., AOD1B, tides, non-tidal atmosphere and ocean). These serve as the input to the unconstrained least-squares gravity inversion used to estimate SH coefficients.
- *Geo-fit* $\left(\delta\dot{\rho}^{(g)}\right)$: Refers to the component of the range-rate signal associated with the fitted pre-fit data, expressible solely in terms of the estimated SH coefficients (up to degree and order 180 in this study). It represents the SH-only contribution to the fitted range-rate signal.
- *Post-fit Residuals* $(\Delta_{\delta\dot{\rho}})$: Denotes the difference between the pre-fit range-rate observations and the total fitted signal from the least-squares fit. These residuals capture the remaining signals that are not explained by the estimated monthly gravity field, background models, and instrument noise.

The following relation is used to summarize what was mentioned above:

$$\delta\dot{\rho} = \delta\dot{\rho}^{(\mathrm{l})} + \delta\dot{\rho}^{(\mathrm{c})} + \delta\dot{\rho}^{(\mathrm{g})} + \Delta_{\delta\dot{\rho}}, \tag{1}$$

where (l), (c) and (g) refer to the local, common and global residual range rate components (Pini, 2012), and $\Delta_{\delta\dot{\rho}}$ is the post-fit range rate residuals. Global parameters are defined as constants applicable to all arcs and data sets, including the estimated SH coefficients. An arc refers to a continuous orbit integration, with each one associated with three distinct data sets: KBR1B (*K*-band Ranging Level-1B), GRACE-A, and GRACE-B GPS data. Common parameters encompass those shared across all models and arcs over a pre-defined period (usually 24 hr), such as the initial state vector, and various accelerometer calibration parameters. Local parameters, on the other hand, pertain to a section of individual arcs, including those related to single GPS satellites (e.g., zenith delays), KBR phase breaks, and others.

This separation of parameters is inherited from the CSR processing strategy and is essential for isolating and identifying the influence of different error sources and modeling choices on the data. Geo-fits are thus a special category of the global parameters model response, purely written in terms of the monthly SH coefficients. This

study concentrates on the high-frequency gravimetric signal content from GRACE residuals, specifically on the post-fit residuals.

2.2. GRACE Daily Gravity Solutions

In this study, we use the ITSG-Grace2018 Kalman-filtered daily solutions (Kvas et al., 2019), as a crucial component for validation our findings on high-frequency mass change phenomena. These solutions come from the most recent version of ITSG's Kalman-filtered gravity data, which are SH coefficients provided up to degree $l_{\max} = 40$ and have a daily temporal resolution. Specifically, we utilize the Level-3 gridded daily solutions provided in NetCDF format (https://ftp.tugraz.at/outgoing/ITSG/GRACE/ITSG-Grace2018/daily_kalman/netcdf/), which are derived from the daily SH coefficients and already converted to Equivalent Water Height| Equivalent Water Heights (EWH) units (cm) by the data provider. Although the spatial resolution is somewhat limited with a (half-wavelength) spatial resolution of 500 km, these gravity field solutions represent the state-of-the-art in terms of temporal resolution.

2.3. Level-4 Altimetry Products

To enhance our understanding and characterization of the post-fit residuals related to high-frequency mass change phenomena occurring over the oceans, we analyzed gridded Sea-Level Anomalies (SLA) from a Level-4 multi-mission altimetry product provided by the E.U. Copernicus Marine Service Information https://doi.org/10.48670/moi-00148. These gridded data are available in netCDF format for the entire period from January 1993 to May 2023, covering the duration of the GRACE mission.

2.4. Meteorological Data

We also utilize publicly available cyclone tracking and rainfall data from the Bureau of Meteorology (BoM) http://www.bom.gov.au/ for our analysis of meteorological high-frequency mass change phenomena. The cyclone tracking data is in CSV format and includes information on all past cyclones, while the rainfall data is presented in a latitude-longitude gridded format and measured in millimeters.

3. Methods

3.1. Typical Acceleration Approach

As a first step, let us recall the geometry of the GRACE system, which consists of two satellites denoted here as A and B, separated by an approximate distance of 220 km in the Line-of-Sight (LoS) direction. To derive the Equation of Motion, an instantaneous relative reference frame is used, with its main directions being LoS, radial, and out-of-plane.

The range ρ, range rate $\dot{\rho}$ and range acceleration $\ddot{\rho}$ can be computed with (Ghobadi-Far et al., 2018)

$$\rho = \mathbf{x}_{AB} \cdot \mathbf{e}_{AB}^{\mathrm{LoS}}, \tag{2}$$

$$\dot{\rho} = \dot{\mathbf{x}}_{AB} \cdot \mathbf{e}_{AB}^{\mathrm{LoS}}, \tag{3}$$

$$\ddot{\mathbf{x}}_{AB} \cdot \mathbf{e}_{AB}^{\mathrm{LoS}} = \ddot{\rho} - \frac{1}{\rho}\left(\dot{\mathbf{x}}_{AB} \cdot \dot{\mathbf{x}}_{AB} - \dot{\rho}^2\right). \tag{4}$$

where $\mathbf{x}_{AB}$, $\dot{\mathbf{x}}_{AB}$ and $\ddot{\mathbf{x}}_{AB}$ are the relative position, velocity and acceleration vectors of the GRACE-A and -B satellite pair (in an Earth-Centered Earth-Fixed frame), and $\mathbf{e}_{AB}^{\mathrm{LoS}}$ is the unit vector in LoS direction. The second term on the right-hand side of Equation 4 is typically referred to as the centrifugal acceleration term (which from now is summarized as g_c).

However, it is evident that the gravity field is still not explicit in the latter equation. This situation can be addressed by using Newton's second law of motion for both A and B, and then taking their difference:

$$\ddot{\mathbf{x}}_{AB} = \mathbf{g}_{AB}^{\mathrm{bkg}} + \delta\mathbf{g}_{AB} + \mathbf{a}_{AB}^{\mathrm{ng}} + \epsilon, \tag{5}$$

where $\mathbf{a}_{AB}^{\mathrm{ng}}$ represents all non-gravitational accelerations, such as air drag and pressure radiation. Meanwhile, $\mathbf{g}_{AB}^{\mathrm{bkg}}$ and $\delta\mathbf{g}_{AB}$ denote the gravity differences between satellites GRACE-A and GRACE-B. Specifically, $\mathbf{g}_{AB}^{\mathrm{bkg}}$ is associated with all known background models, $\delta\mathbf{g}_{AB}$ reflects the time-variable gravity signal of interest, and $\boldsymbol{\epsilon}$ accounts for residual contributions from the static gravity field, background model imperfections, and instrument errors.

To derive the residual range rate variables that we use in this study, CSR applied background models related to the static gravity field (GGM05C), the de-aliasing AOD1B RL06 product (Flechtner, 2007), and other (non-)tidal and non-gravitational accelerations. For more information on the background models and processing strategy implemented by CSR, the reader is referred to (S. V. Bettadpur, 2018). Residual quantities resulting from removing these orbital and background models will be denoted with δ. Thus, by combining both Equations 4 and 5 (projected onto the LoS direction), the resulting residual relation is

$$\delta g_{AB}^{\mathrm{LoS}} = \delta\ddot{\rho} + \delta g_{\mathrm{c}} + \epsilon, \tag{6}$$

where $\delta g_{AB}^{\mathrm{LoS}}$ and δg_{c} are the residual Line-of-Sight Gravity Difference (LGD) and centrifugal term, respectively.

3.2. From Range Rate to Line-of-Sight Gravity Difference Residuals

It is important to note that we are provided with residual range rates, denoted as $\delta\dot{\rho}$. There is no straightforward method to compute δg_{c} without performing the extensive orbital modeling done by CSR. Additionally, one of the goals of this study is to demonstrate the effectiveness of this intermediate GRACE product, which is always produced when generating unconstrained Level-2 gravity solutions. Therefore, we follow three steps to obtain the residual LGDs from the residual range rates.

First, we start by applying a Butterworth low-pass (zero-phase) filter (of order 3) to the residual range rates to eliminate the high-frequency noise introduced by the KBR instrument noise, using a cutoff frequency of 11 mHz. This is necessary because noise begins to dominate the signal at this frequency (Ghobadi-Far et al., 2018; Goswami, 2018; Peidou et al., 2022). Additionally, we need to remove long wavelengths that can obscure geophysical signals at frequencies below 0.9 mHz (Ghobadi-Far et al., 2018). As a result, we also apply a high-pass filter. This combined filtering approach effectively creates a band-pass filter with a characteristic frequency range of (0.9, 11) mHz, roughly corresponding to SH degrees 5 to 60, where geophysical signals are present. Filtering is performed in the temporal domain by first segmenting the time series based on data gaps, defined here as interruptions longer than 20 s (four missing samples). The band-pass filter is then applied separately to each continuous segment. To mitigate edge effects, we tested several strategies (e.g., zero-padding, symmetric reflection), but their impact was found to be negligible, particularly after spatial binning, where such effects tend to average out.

Secondly, we apply a fourth-order accurate central numerical differentiation scheme (with $n = 2$), in the form of a convolution of $w_{i,j}$ parameters which can be obtained by an iterative process presented below (Khan & Ohba, 1999):

$$w_{1,2n} = \frac{n}{n+1}, \tag{7}$$

$$w_{k,2n} = -w_{k-1,2n}\frac{(k-1)(n-k+1)}{k(n+k)}, \quad k = 2,3,4,\ldots,n, \tag{8}$$

$$w_{-l,2n} = -w_{l,2n}, \quad l = 1,2,3,\ldots,n. \tag{9}$$

Note the central coefficient is set to $w_{0,2n} = 0$. At the edges of each data section, a forward and backward scheme is applied to ensure that we do not have any edge-related numerical errors caused by the central scheme.

We now have at our disposal a band-pass filtered residual range acceleration time-series, $\delta\ddot{\rho}(t)$, which has been widely used as an approximation of LGD (e.g., by Allgeyer et al. (2022); Killett et al. (2011); Spero (2021); Weigelt (2017)), however by removing the centrifugal residual, one can better localize mass anomalies on the

Earth's surface (Ghobadi-Far et al., 2018). Thus, as a third and final step, an analytical transfer function, $Z(f)$, is applied on $\delta\ddot{\rho}$ as follows (Ghobadi-Far et al., 2018)

$$\delta g_{AB}^{\mathrm{LoS}}(t) = \mathcal{F}^{-1}\left\{Z(f)\mathcal{F}\left\{\delta\ddot{\rho}(t)\right\}\right\} + \Delta_{g}, \tag{10}$$

where f is the frequency, $\mathcal{F}$ is the Fourier transform, Δ_{g} is the transfer function error related to the centrifugal term, and lastly the transfer function analytical fit is (Ghobadi-Far et al., 2018)

$$Z(f) = 1 + 3.45 \times 10^{-4} f^{-1.04}. \tag{11}$$

The use of this empirical function leads to an accuracy improvement from 50% to 70% compared to the typical residual range acceleration approximation, where the global root mean square (RMS) of the band-passed filtered Δ_{g} was found to be below 0.2 nm/s^2 (Ghobadi-Far et al., 2018). Applying this transfer function is therefore an essential processing step to improve the accuracy of our geophysical analysis.

3.3. Spatial-Temporal Linear Regression

One of the main contributions of this paper is the characterization of the sub-monthly content in post-fit residuals. For this purpose, we first perform binning onto a rectangular grid of the data and perform a linear temporal parametrization per grid cell of the sub-monthly gravity signal in post-fit residuals. Thus, in each grid cell described by the longitude-latitude pair (λ_0, θ_0), we assume the following relationship:

$$\delta g_{AB}^{\mathrm{LoS}}(\lambda_0, \theta_0, t) \approx a(\lambda_0, \theta_0)(t - t_{\mathrm{mid}}) + b(\lambda_0, \theta_0), \tag{12}$$

where a and b represent the trend and bias (at time $t = t_{\mathrm{mid}}$), respectively. Here, t_{mid} denotes the midpoint of the month over which the regression is performed. These parameters are computed using the known regression equations:

$$a = \frac{n\sum_i^n \left(t_i \left(\delta g_{AB}^{\mathrm{LoS}}\right)_i\right) - \sum_i^n t_i \sum_i^n \left(\delta g_{AB}^{\mathrm{LoS}}\right)_i}{n\sum_i^n t_i^2 - \left(\sum_i^n t_i\right)^2}, \tag{13}$$

$$b = \frac{\sum_i^n \left(\delta g_{AB}^{\mathrm{LoS}}\right)_i - a\sum_i^n t_i}{n} + a t_{\mathrm{mid}}, \tag{14}$$

where t_i and $\left(\delta g_{AB}^{\mathrm{LoS}}\right)_i$ denote the timestamp (in seconds) and corresponding LGD value of the i-th data point within a given month and grid cell, with n being the total number of available data points in that cell. Grid cells with no data points during the month are excluded from the regression.

The results from Equations 13 and 14 yield the spatial monthly distributions of the linear representation of the sub-monthly gravity field and other non-gravitational residuals, as discussed in previous sections. Although sub-monthly variations due to phenomena such as floods or cyclones can be non-linear in time, we observed that the post-fit residuals often exhibit persistent shifts, either from negative to positive, or vice versa, relative to the monthly baseline. In this context, fitting a linear trend provides a simple yet effective way to capture these anomalies across space and time. More complex temporal models are beyond the scope of this study.

4. Analysis of KBR Residual Level-1B Data in the Context of High-Frequency Mass Change Variations

High-frequency mass change phenomena occur across various spatial and temporal scales, driven by processes within the atmosphere, oceans, land hydrology, and the solid Earth. These mass change signals can be observed and characterized using GRACE gravimetry data. In this study, we focus on analyzing post-fit residuals in the form of Line-of-Sight Gravity Differences (LGDs).

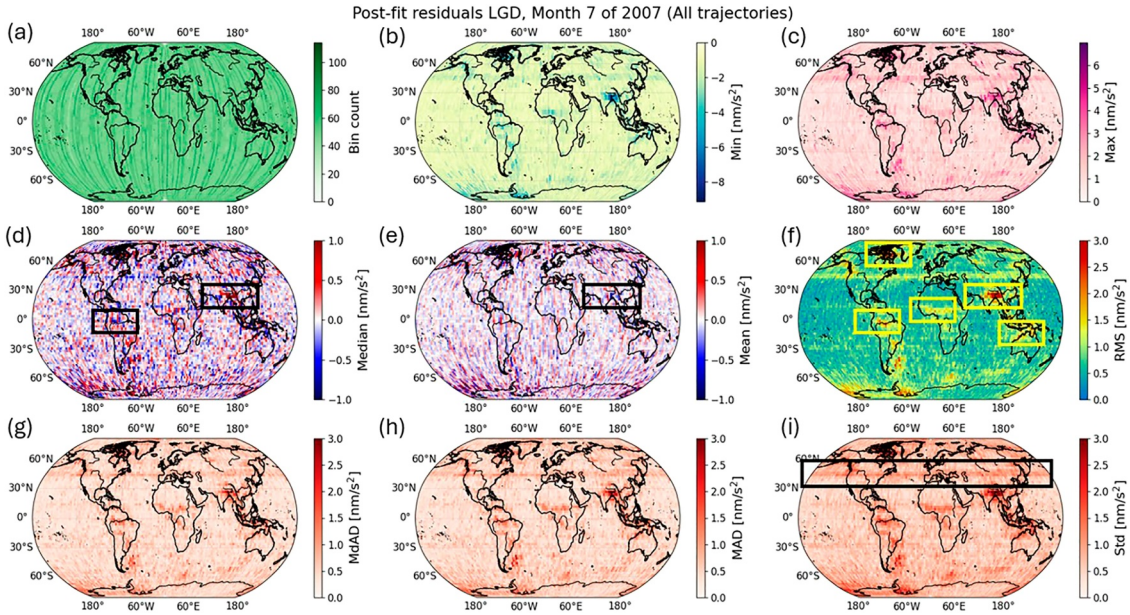

Figure 1. Spatially binned (2.5° × 2.5°) statistical layout of Line-of-Sight Gravity Difference post-fit residuals for the month of July 2007. Top row: (a) bin count, (b) minimum, and (c) maximum. Middle row: (d) median, (e) mean, and (f) root mean square. Bottom row: (g) median absolute deviation, (h) mean absolute deviation, and (i) standard deviation (std).

4.1. Global Overview of High-Frequency Mass Change Phenomena

In this section, we present an overview of the major categories of high-frequency change signals and characterize their spatial distribution.

4.1.1. Statistics of Post-Fit Residuals

To visualize the signal content in post-fit residuals, a spatial analysis is performed. By "spatial," we mean that the data is binned into latitude-longitude grids, and several statistics are computed based on the data points falling within these bins.

We observed that the spatial RMS, as well as other statistical variance estimators and linear regression parameters (see Section 4.1.2), such as standard deviation and median/mean absolute deviations (Median Absolute Deviation (MdAD) and Mean Absolute Deviation (MAD) respectively), of the post-fit residuals, offer an optimal way to visualize the different types of high-frequency signals, as opposed to other statistical measures such as the spatial mean or median. To explain this, two randomly selected monthly statistical layouts of binned GRACE post-fit residuals are presented in Figure 1 (07/2007) and 2 (10/2014).

Two general observations emerge from the plots. First, while the binned mean (Figures 1e and 2e) post-fit LGDs show no particular pattern, the median values (Figures 1d and 2d) exhibit more structure, especially noticeable in regions such as South Asia, Central Africa, and the Amazon basin. Secondly, the variance plots—including standard deviation, MAD, and MdAD—along with the RMS and maximum values (Figures 1 and 2b, 2c, 2f, 2g–2i), display structures that correlate with sub-monthly geophysical phenomena (geographically constrained, coherent, and persistent signals) and other mis-modeled artifacts. We hypothesize that an example of accelerometer artifact is particularly evident in the post-fit residuals RMS and the variances of 1 nm/s^2 observed as a continuous 45°N latitudinal band, as shown in Figure 1i. This band cannot be explained by any geophysical phenomenon and as it correlates with the spatial patterns of monthly inter-satellite pointing pitch variations presented by Bandikova et al. (2012), we hypothesize that these are residual thruster accelerometer signals (Bandikova et al., 2019). These and other accelerometer remnants (i.e., roll, yaw and combined variations) seem to be present throughout the majority of post-fit residuals' plots during the GRACE mission (not shown).

The difference between the median/mean statistics (e.g., Figures 1d and 1e), which show little to no geophysical correlation, and the RMS and variances, which do exhibit such correlations, can be explained by the nature of the

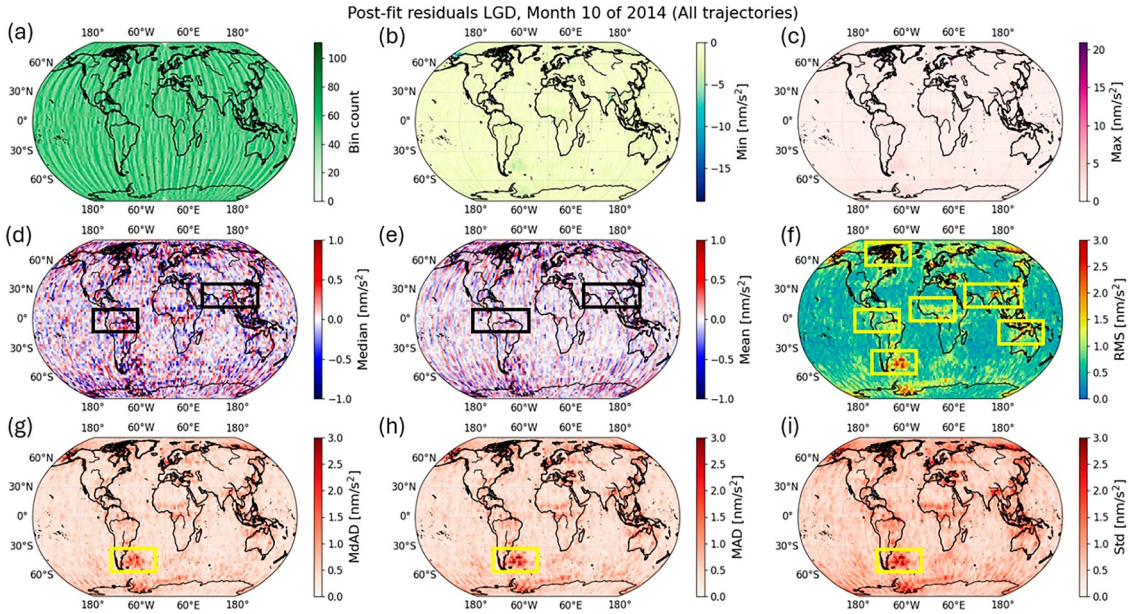

Figure 2. Spatially binned (2.5° × 2.5°) statistical layout of Line-of-Sight Gravity Difference post-fit residuals for the month of October 2014. Top row: (a) bin count, (b) minimum, and (c) maximum. Middle row: (d) median, (e) mean, and (f) root mean square. Bottom row: (g) median absolute deviation, (h) mean absolute deviation, and (i) standard deviation (std).

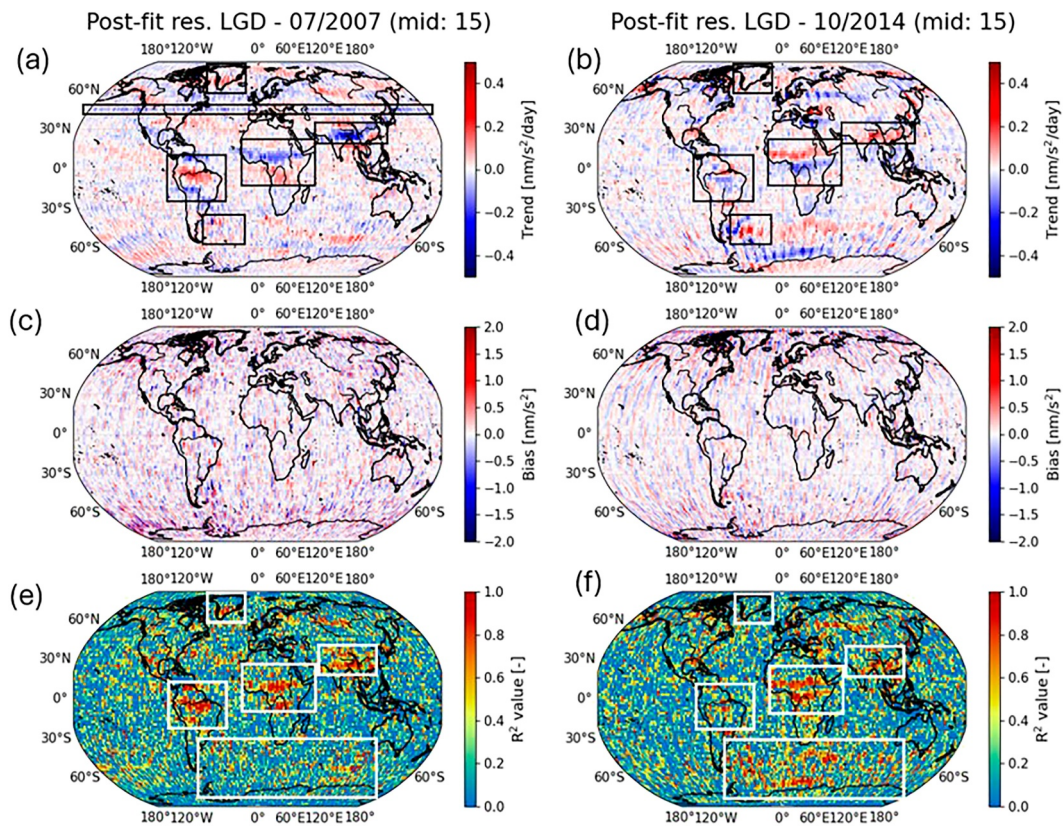

Figure 3. Spatio-temporal linear regression grid (2° × 2°) showing Line-of-Sight Gravity Difference post-fit residuals for the month of July 2007 (left) and October 2014 (right). (a) and (b): trend in (nm/s^2)/day, (c) and (d): bias at 15 days in nm/s^2, and (e) and (f) adjusted R^2-value.

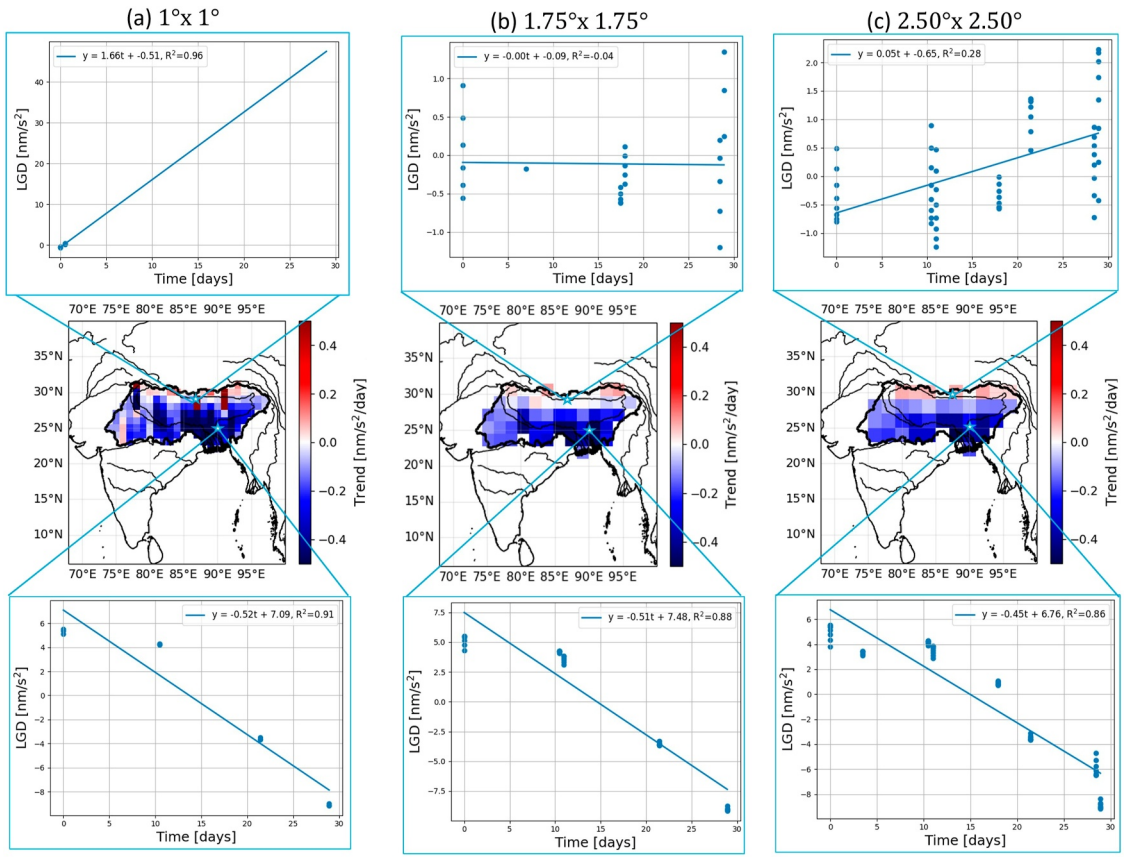

Figure 4. Linear regression trends depicted in a grid format for three distinct grid sizes, analyzing time series data for two specific grid cells during July 2007. The grid sizes include: (a) 1° × 1°, (b) 1.75° × 1.75°, and (c) 2.5° × 2.5°. This analysis illustrates variations in trends across different spatial resolutions.

post-fit residuals. These residuals indicate mass anomalies relative to the monthly solutions (geo-fit), leading them to oscillate around the monthly average, causing them to superimpose and cancel each other out, resulting in a lack of any discernible pattern. In contrast, the amplitude of these oscillations is captured by analyzing the power of the signal (RMS) or by examining their absolute or squared deviations (MAD or MdAD). Due to this, the RMS will be used throughout this paper to visualize the power of GRACE's unmodelled reduced observations of sub-monthly signals.

4.1.2. Temporal Characteristics of Post-Fit Residuals

Following the description of the simple binning statistics of the GRACE post-fit residuals, we now present the temporal characterization for the same 2 months mentioned earlier. This is illustrated in Figure 3, using the temporal linear regression parameterization described in Section 3.3.

Several observations can be made from Figure 3. First, regions with high spatial RMS, as shown in Figures 1f and 2f, correspond directly to areas that exhibit distinct trend signals in Figures 3a and 3b. Notably active river basins, such as the Amazon and Ganges-Brahmaputra, show trend values of up to ±0.5 nm/s^2/day. Additionally, African basins like the Niger, Chad (South) Nile, and Congo exhibit trend values of ±0.25 nm/s^2/day. Furthermore, the mid-month LGD bias presented in Figures 3c and 3d does not show any discernible geophysical patterns, as the values remain below ±0.5 nm/s^2. This indicates that the sub-monthly characteristics of post-fit residuals can be sufficiently described by a linear trend alone and that the monthly SH solutions do not have any bias in these regions. Thus, this would suggest that the monthly solutions have absorbed the dominant low-frequency components. Finally, the large trend values result in LGD sub-monthly variations of up to 15–20 nm/s^2 throughout the month, corresponding to more than half the magnitude of the monthly signals.

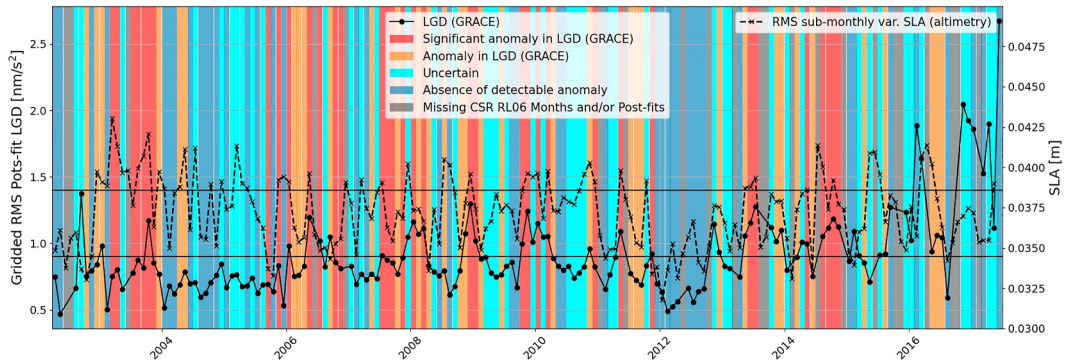

Figure 5. Time series of gridded root mean square (RMS) LGD post-fit residuals, and RMS sub-monthly variability of daily gridded sea-level anomalies in the Zapiola region for the entire duration of the gravity recovery and climate experiment mission. A qualitative assessment, indicated by color bands into four categories: absence (blue), uncertain (cyan), anomaly (orange), and significant anomaly (red), is shown to determine whether the observed signals are due to high-frequency mass variations. Finally, the threshold range of (0.92, 1.42) nm/s^2 is illustrated as solid horizontal lines.

Second, these river basins (highlighted in Figures 3e and 3f) show the highest R^2 values (from 0.7 to 0.98), while the northern oceanic regions display low R^2 values (below 0.5). This indicates that sub-monthly land hydrology, caused by sudden events such as floods and heavy precipitation, can be identified and characterized using spatially distributed linear regression. Meanwhile, the southern oceanic regions demonstrate higher sub-monthly activity than expected (Bonin & Save, 2020; Schindelegger et al., 2021). In contrast, the northern oceanic regions exhibit low R^2 values, which may be due to the relatively low magnitude of sub-monthly signals in these areas (Peidou et al., 2022). Such weak signals can be further obscured by residual KBR noise (Peidou et al., 2022), reducing the correlation strength and making it more difficult to capture meaningful geophysical trends.

Thirdly, this methodology also allows us to identify unmodeled AOD1B and ocean tidal signals related to ocean currents in Figures 3b and 3f, particularly associated with the sub-tropical gyre in the Argentine basin. Finally, we can distinguish the positive sub-monthly trend of 0.1 nm/s^2/day in southern Greenland during the summer month of July 2007 (which is not observed during the autumn month of October 2014 in Figure 3b). This trend is likely associated with rapid ice sheet melting, which leads to mass redistribution and increased gravitational signals detectable by GRACE. Additionally, we observe the hypothesized accelerometer remnant with a trend of −0.08 nm/s^2/day along the 45°S latitudinal band in Figure 3a. These results related to the linear regression of post-fit residuals suggest that it is possible to improve the high-frequency resolution of monthly models. By incorporating geo-fits and post-fit residuals, sub-weekly solutions could be easily generated through interpolation. However, this study primarily focuses on characterizing these signals rather than reconstructing higher-resolution solutions, making such improvements beyond its current scope.

Finally, we verify our linear regression strategy by focusing on the time series of two grid cells for July 2007 within the Ganges-Brahmaputra river basin in Figure 4.

In the top and last row of Figure 4, increasing the grid size results in a greater number of data points and their corresponding arc passings. This increase in data points introduces more variability within each arc passing, as satellite tracks sample different parts of the gravity field at slightly different times. Consequently, as the grid cell size increases (Figures 4a–4c), short-term along-track fluctuations become more pronounced due to the inclusion of more along-track points with slightly different temporal characteristics. However, in regions with a clear trend, this added variability does not significantly alter the final trend estimate. Notably, the top row highlights several large artifacts, particularly in Figure 4a, where the limited number of data points within a small grid cell results in an artificially high trend value of 1.66 nm/s^2/day. As the grid cell size increases, more arc passings contribute to the estimate, mitigating these extreme values and providing a more stable trend representation.

Although Figure 4c hints at a possible quadratic drift, we apply linear regression uniformly across all cells to maintain consistency and avoid over-fitting, especially in sparsely sampled regions. This highlights a key advantage of our chosen approach: by selecting a moderate grid cell size of 1.75° for both latitude and longitude,

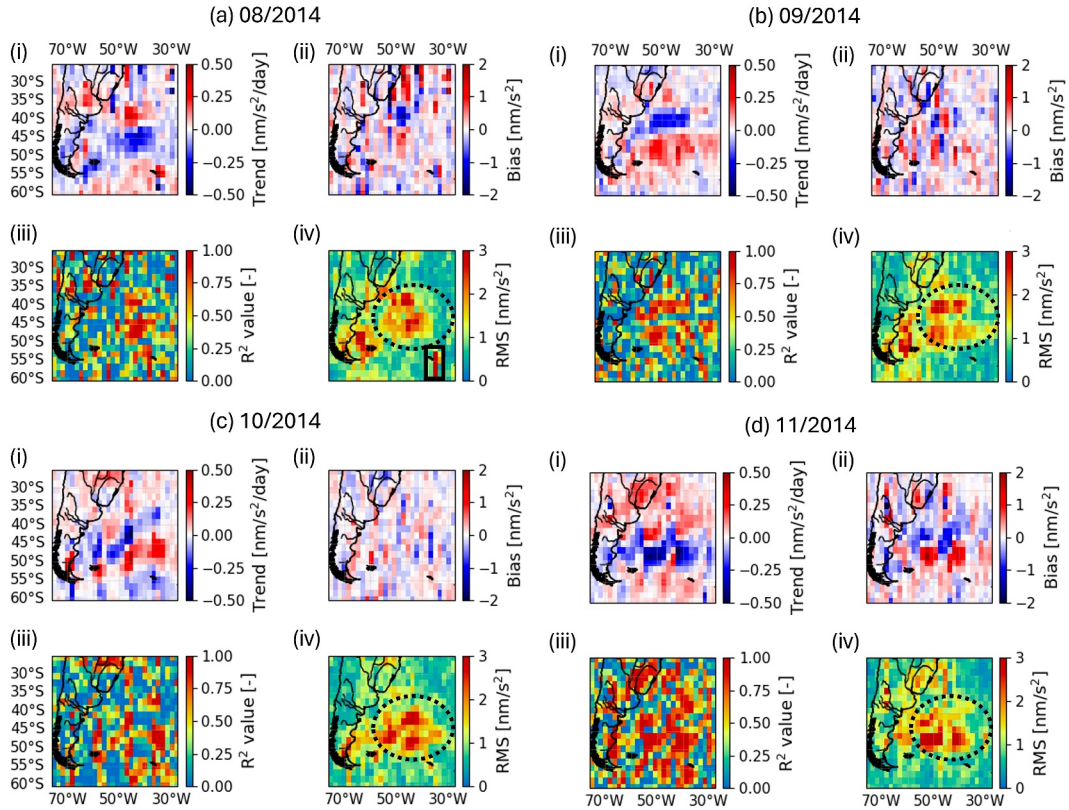

Figure 6. Four consecutive monthly grid groupings displaying spatially binned (1.75° × 1.75°) Line-of-Sight Gravity Differences (LGD) post-fit residuals and their linear regression results for the months of August (a) to November 2014 (d) in the Zapiola region with sub-plots (i): trend, (ii): mid-month bias, (iii): adjusted R^2-value, and (iv): spatially binned root mean square.

we balance the need for spatial resolution with statistical robustness. The definitive optimization of grid cell size and mesh is considered beyond the scope of this work.

4.1.3. Sub-Monthly Geophysical Signals

Our general analysis of all monthly GRACE post-fit residuals solutions (such as Figures 1–3) reveals two primary categories of high-frequency signals, which is in strong agreement with previous studies (Ghobadi-Far et al., 2020, 2022; Peidou et al., 2022):

1. *Hydro-meteorological and Oceanic processes:* Unmodelled phenomena in background AOD1B and ocean tidal products, particularly in terms of atmospheric and oceanic mass change, is a significant source of high-frequency signals (Bonin & Save, 2020; Ghobadi-Far et al., 2022; Schindelegger et al., 2021). This is especially evident in the global oceans, where residuals indicate unmodeled effects from short-term variability in oceanic currents and pressure systems, such as the mass anomalies related to the Zapiola region in the Argentine basin as can be seen highlighted from the RMS (and other variance plots) post-fit residuals in Figures 2f–2i.
2. *Land Hydrology:* Sub-monthly land hydrology signals are particularly prominent in regions with large river basins, such as the Amazon, central Africa and South Asia (see in particular the large variabilities in Bangladesh and India highlighted in Figure 1f). Here, rapid changes in water storage due to precipitation and river discharge (e.g., during monsoon seasons) contribute to the high-frequency mass change.

In this study, we only focus our analysis on these two general categories. Solid Earth processes, specifically the resulting tsunami loadings after the December 2004 Sumatran and March 2011 Tohoku earthquakes were observed in LGD residuals (Ghobadi-Far et al., 2020). Lastly, glaciology is also regarded as outside the scope of this study. To date, we have not found any research on the sub-monthly characteristics of LGD or range-rate

residuals in polar regions. This absence of studies may be due to the fact that glaciology involves relatively slower geophysical processes, mostly characterized by seasonal variations. Both categories will be considered for future research.

Our findings support the results of the previously mentioned studies. However, we significantly expand upon those results in the following sections by providing a detailed spatial and temporal characterization of specific examples of rapid mass change phenomena throughout the entire duration of the GRACE mission.

4.2. Oceanic High-Frequency Mass Change Signals

The Zapiola region, situated within the Argentine Basin in the South Atlantic Ocean off the coast of Argentina (centered at 44°S 45°W), is a unique and dynamically active area characterized by intense oceanic currents and mass change. This region hosts the Zapiola Anticyclone, a large, clockwise-rotating, deep-reaching current system that forms over the Zapiola Rise—an elevated underwater plateau. The anticyclonic circulation around the Zapiola Rise traps water masses and sediment, leading to highly concentrated mass anomalies (de Miranda et al., 1999; Volkov & Fu, 2008).

In terms of high-frequency mass change, the Zapiola region is significant due to the strong currents and complex interactions between the water column and seabed, which create rapid and localized mass variations. These fluctuations produce measurable, sub-monthly signals in gravimetric data, such as a dipole-like barotropic mode which rotates with a 20–25 days period already detected by Han et al. (2014); Yu et al. (2018) using 10-day GRACE solutions (Lemoine et al., 2007). Furthermore, Ghobadi-Far et al. (2022) showed that localized anomalies detected by altimetry, in the form of SLA, could explain along-orbit LGD residual variations in Laser Ranging Interferometry L1B observations.

We conduct the first system-level characterization (without engaging in physical modeling of ocean circulation processes) of the oceanic gyre high-frequency signals by calculating the monthly mean of the spatially gridded RMS post-fit residuals over the region defined by (35°–55°S; 27.5°–55°W) for the entire duration of the GRACE mission, as shown in Figure 5. Each point in the solid line curve of Figure 5 represents the magnitude of the unmodelled geophysical high-frequency signals, which has its most likely source in errors of the AOD1B and other background models, with the addition of other artifacts such as initial state vector, and accelerometer errors.

Furthermore, we performed a qualitative assessment through a heuristic visual inspection approach of all monthly post-fit residual plots (which are provided in Supporting Information S1). These plots are represented by arbitrarily chosen color bands that range from significant anomalies to uncertain variations and even the absence of anomalies. This classification allows for an initial visual interpretation of potential signal patterns. Based on this categorization, we then quantified the detection rate by counting the number of months classified as a " (significant) anomaly" for which the RMS falls within the specified interval. This interval was established by maximizing the detection rate while minimizing the occurrences of no anomalies detected.

It is important to note that, despite the limitations inherent in the visual qualitative assessment, this analysis serves as a preliminary step toward contextualizing the magnitude of mean RMS post-fit residuals. Specifically, it highlights that a post-fit residual signal RMS may also represent sources beyond unmodelled AOD1B, such as various accelerometer artifacts (see previous section). The observed increase in RMS since mid-2016 corresponds with the final GRACE era, during which the satellites relied on only one accelerometer.

We found that within a mean gridded RMS interval of (0.92, 1.42) nm/s^2 (represented as two horizontal lines in Figure 5), the detection rate is 74%. This indicates the presence of a consistent geophysical signal during that month. The associated probabilities for the classification being labeled as "uncertain" and for a lack of detection are 21.7% and 4.3%, respectively. The associated statistics of this classification analysis can be found in (Figure S1 in Supporting Information S1). Using the presented approach, we identify the period from August–November 2014 (see the peak categorized as "significant anomaly" in Figure 5) showing significant sub-monthly variabilities of which spatial maps can be found in Figure 6.

Figure 6 (mainly shown in the trend and RMS (i) and (iv) subplots) shows tidal mis-modelings, which are typically observed in shallow waters, near the coast within the Patagonian shelf (from 45° to 55°S). Additionally, constant longitudinal artifacts such as the large deviations caused by the mis-modeled initial state vector from Figure 6aiv in August 2014 have been highlighted on the south-eastern side. Most significantly, the evolution of

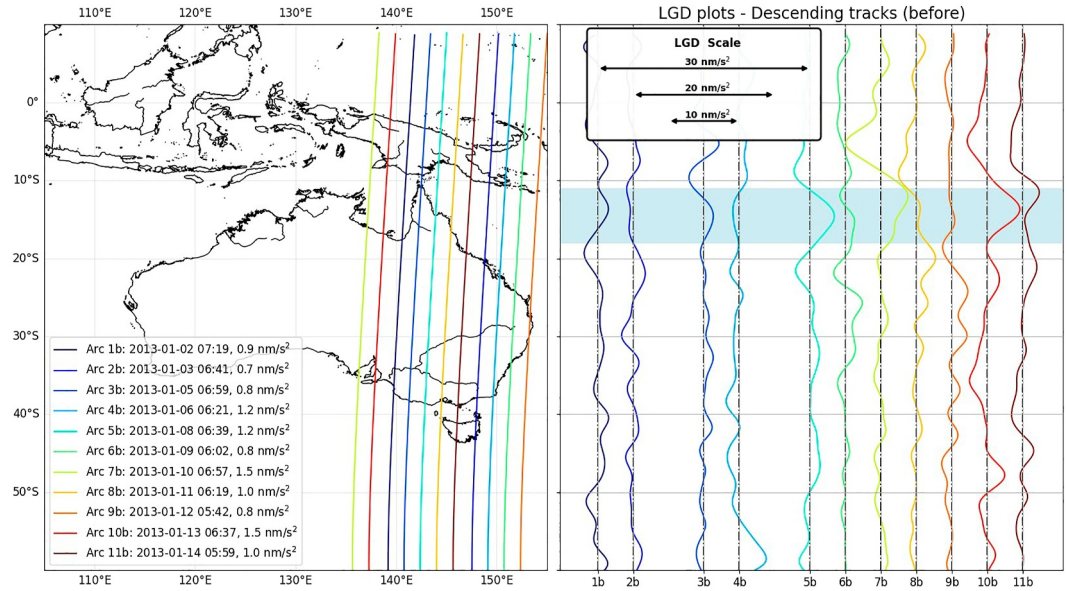

Figure 7. *Left*: Ground tracks from the gravity recovery and climate experiment mission, descending arcs (1–11b), displayed alongside their corresponding initial dates (prior to Cyclone Oswald) and the associated Line-of-Sight Gravity Difference (LGD) root mean square values. *Right*: Along-orbit LGD post-fit residuals plotted against latitude for the indicated arcs (1–11b), with a LGD scale included. The spacing along the *x*-axis is proportional to the time interval between each consecutive track.

sub-monthly mass change is primarily characterized by a rotating pair of negative-positive trend mass anomalies in all (i) sub-plots of Figure 6. These reach values similar to land hydrology up to ±0.5 nm/s^2/day. Furthermore, apart from November 2014 (Figure 6dii), the mid-month bias does not show any significant geophysical signal. These anomalies appear to rotate around the Zapiola Rise and be constrained by the topography of the Argentine

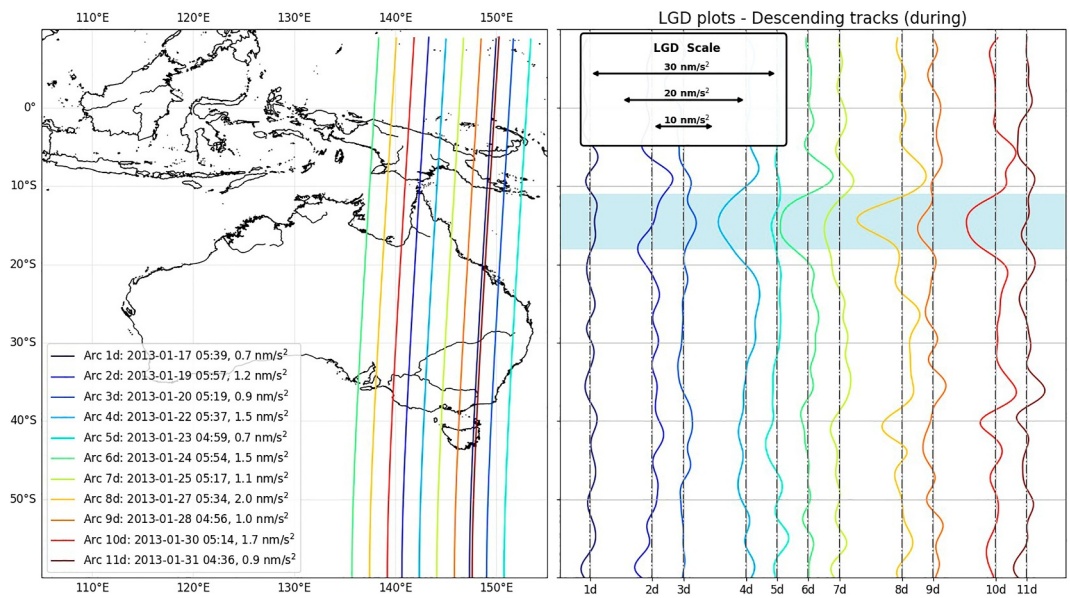

Figure 8. *Left*: Ground tracks from the gravity recovery and climate experiment mission, descending arcs (1d–11d), displayed alongside their initial corresponding dates (during Cyclone Oswald) and the associated Line-of-Sight Gravity Difference (LGD) root mean square values. *Right*: Along-orbit LGD post-fit residuals plotted against latitude for the indicated arcs (1d–11d), with a LGD scale included. The spacing along the *x*-axis is proportional to the time interval between each consecutive track.

basin. Consequently, we interpret that they are linked to high-frequency components of the known dipole-like rotating mode (de Miranda et al., 1999; Yu et al., 2018).

Lastly, we compared this RMS time-series with the sub-monthly variations of Level-4 SLA as provided by the E. U. Copernicus Marine Service Information. The RMS sub-monthly variability (or temporal standard deviation) is calculated using the following equation:

$$RMS_{\text{var}}(\lambda,\ \theta) = \sqrt{\frac{1}{N}\sum_{i=1}^{N}(x_i(\lambda,\ \theta) - \bar{x}(\lambda,\ \theta))^2}, \tag{15}$$

where N represents the number of gridded daily SLA solutions x_i within a specific month, and $\bar{x}$ is the average of all these solutions for that month. The result of Equation 15 is a grid that depicts the RMS variability of the gridded variable x_i in relation to its monthly average. The resulting spatial maps from August–November 2014 can be found in the SI (Figures S2 in Supporting Information S1) and the respective time-series is plotted with the post-fit residuals in Figure 5.

Our comparison revealed no significant temporal correlation coefficients (below 0.25) between the post-fit residuals LGD RMS and the sub-monthly RMS SLA variability time-series (as can be visually observed in Figure 5). To assess the robustness of these results, we recalculated the correlations after excluding all data prior to June 2003 and after August 2016, in order to eliminate potential issues stemming from the initial problematic periods when one SCA (Star Camera Assembly) was malfunctioning and when only one accelerometer was collecting measurements, respectively. Additionally, we segregated the analysis by orbital track type, examining ascending and descending tracks separately. The exclusion of data provided an overall increase of 0.1 (or 50%). In contrast, the adjustments related to orbital track type led to significant variations from only 0.05 (20%) to even 0.15 (75%) in the correlation coefficients, with a maximum value of 0.31 (for ascending tracks). Due to the high sensitivity of low correlation coefficients, spatially averaged SLA variations alone do not adequately explain the high-frequency signals observed by GRACE. This highlights the limitations of such monthly aggregate statistical analyses. As noted by Ghobadi-Far et al. (2022), for specific ground tracks, the along-orbit LGD residuals exhibited (anti-)correlations with daily SLA variations. Furthermore, it is known that the barystatic (mass-related) component of SLAs dominates the region, while the steric component—driven by variations in temperature and salinity—contributes less than 10% to the overall regional signal (Hughes et al., 2007). Consequently, this suggests that other underlying phenomena, such as rapid pressure fluctuations and circulation variations (Ghobadi-Far et al., 2022), may be occurring, which appear to be diminished by the spatiotemporal averaging process.

4.3. Hydro-Meteorological High-Frequency Mass Change Signals

We focus now on the Gulf of Carpentaria (GoC), a shallow sea situated in northern Australia, as our primary case study to examine abrupt hydro-meteorological changes that can be measured using GRACE residual L1B data. This sea is characterized by significant annual variations, with a measurable change in sea surface height of up to 0.4 m, as detected by GRACE Level-2 data (Tregoning et al., 2008). In addition to these annual and seasonal fluctuations, the region exhibits considerable levels of sub-monthly variability (Ghobadi-Far et al., 2022; Schindelegger et al., 2021), which appear to correlate with pressure variations resulting from cyclonic activity (Ghobadi-Far et al., 2022).

During the GRACE period, Cyclone Oswald emerged in the GoC on 17 January 2013, leading to considerable flooding in the Northern Territory and Queensland along its western coast by 29 January (Bureau of Meteorology, 2013). In this study, we investigate this event by analyzing post-fit residuals to offer a gravimetric characterization of the sub-monthly variations induced by the cyclone's occurrence.

4.3.1. Along-Orbit Analysis

We start by presenting the (arbitrarily chosen) descending along-orbit variations of the post-fit residuals as a function of latitude next to their ground-tracks, which is a visualization similar to previous research (Ghobadi-Far et al., 2022; Han, Ghobadi-Far et al., 2021), and is illustrated in Figures 7 and 8, approx. two weeks before and during Cyclone Oswald respectively. The letters “b” and “d” are appended to the arc indices to differentiate between the “before” and “during” tracks, respectively.

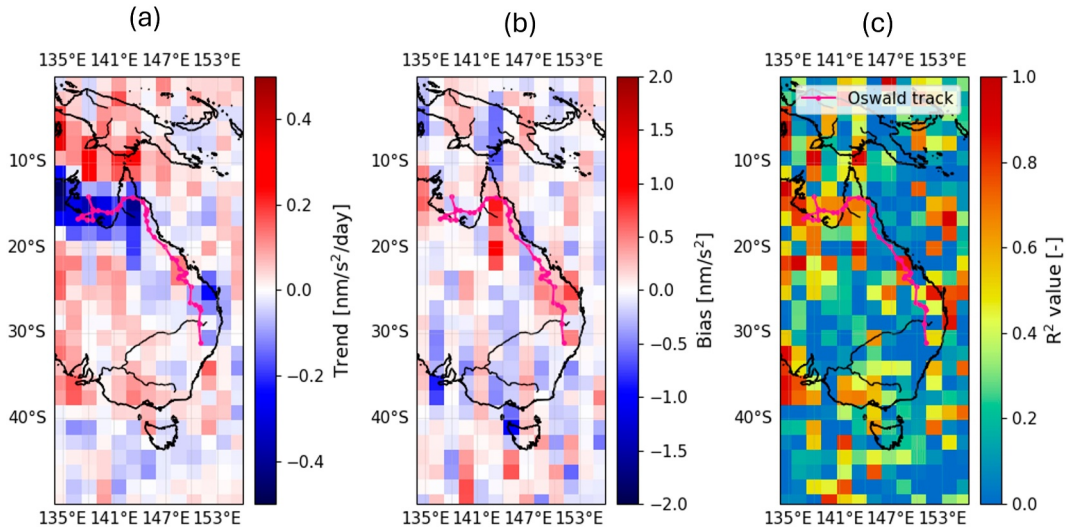

Figure 9. LGD post-fit residuals gridded linear regression (1.75° × 1.75°), with (a) Trend in (nm/s^2)/day, (b) Mid-month bias (nm/s^2), and (c) Adjusted R^2-value. Added to each subplot is the cyclone Oswald's track.

We first focus on the GoC sea near the Northern Territory (where Oswald originated from), where GRACE passed over during arcs 1, 7, and 10b before Cyclone Oswald, as illustrated in Figure 7. In contrast, during the cyclone's occurrence, GRACE directly traversed above it in arcs 6d, 8d, and 10d, shown in Figure 8. Notably, the arc RMS values observed during Cyclone Oswald, at 1.5, 1.7, and 2 nm/s^2, are higher than those recorded before (ranging from 0.9 to 1.5 nm/s^2), with arcs 8d and 10d exhibiting the highest RMS values, reaching up to 2 nm/s^2. These two arcs exhibit negative LGD variations which peak at 15°S latitude of −7.5 nm/s^2 and −5 nm/s^2, respectively. The negative values suggest the presence of sub-monthly positive mass anomalies resulting from pressure differences during Oswald, which were not accounted for in the AOD1B RL06 background model (Ghobadi-Far et al., 2022). At similar latitudes (12°–17.5°S), positive LGD deviations are noted for arcs 7 and 10b, indicating a mass deficit relative to the monthly average. This demonstrates that the monthly solutions have captured a portion of the mass

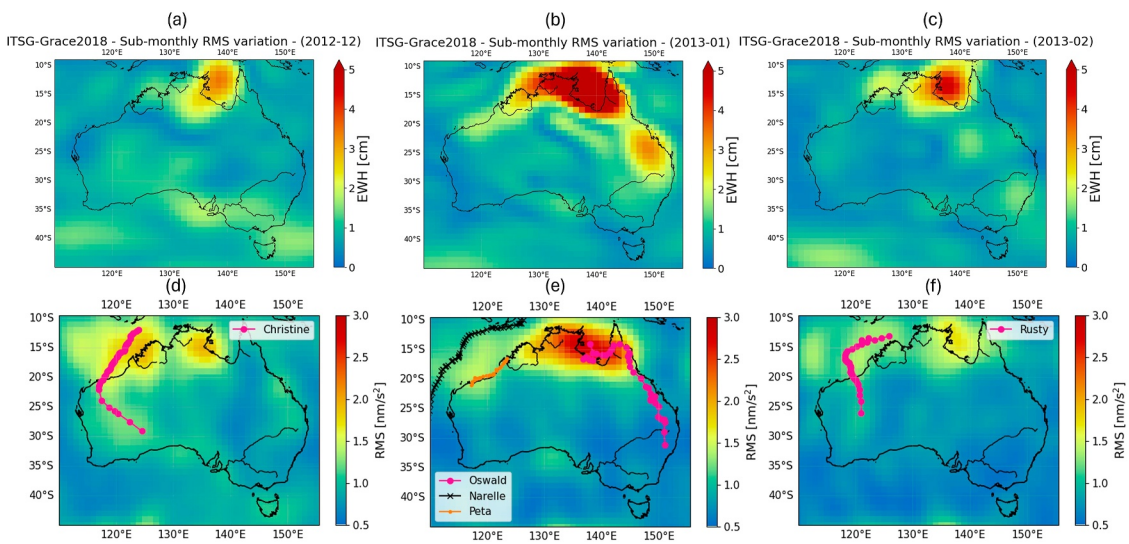

Figure 10. Consecutive monthly grids for December 2012 to February 2013 (left to right) in Australia. The top row (a to c) presents the sub-monthly variations in equivalent water height in cm of daily Kalman filtered solutions from ITSG-Grace2018, and the bottom row (d to f) shows the gridded and spatially smoothed (Gaussian filter with radius 6° and $\sigma = 2$) LGD post-fit residuals root mean square (1° × 1°). The cyclone tracks for each month have been added: Christine (December 2012), Oswald, Narelle, and Peta (January 2013), and Rusty (February 2013).

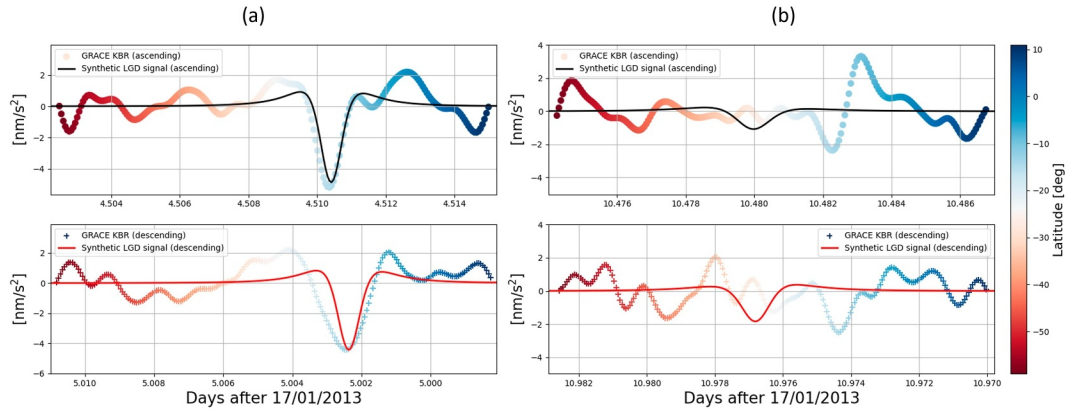

Figure 11. Two examples of along-orbit post-fit LGD residuals (denoted as "GRACE KBR"), compared to synthetic LGDs from a 30 Gt-point mass model of the Oswald cyclone (solid line). The bottom row shows descending tracks (the time-axis is inverted), whereas the top row presents ascending tracks. (a) Example of alignment between synthetic and post-fit residuals LGDs. (b) Example of complete misalignment between synthetic and post-fit residuals LGDs.

(pressure) variation signals induced by Oswald, revealing an overestimation in mass prior to the cyclone's impact, as indicated by the post-fit residuals.

We conducted a parallel analysis for the ascending tracks and observed comparable results (see Figures S3 and S4 in Supporting Information S1); specifically, the transition from slightly positive to substantially negative LGD variations, reaching up to -5 nm/s^2, occurred from the period preceding Oswald to during its presence. These observations underscore GRACE's capability to detect instantaneous mass deficits/excess w.r.t. the monthly average associated with extreme weather events, consistent with the prior study by Ghobadi-Far et al. (2022) that highlights its sensitivity to transient mass redistribution caused by atmospheric pressure changes.

4.3.2. Spatial Analysis

After examining individual trajectories over the GoC, we will now analyze the overall spatio-temporal variations using linear regression on the post-fit residuals, as illustrated in Figure 9. In Figure 9a, we observe a significant LGD trend ranging from -0.1 to -0.3 nm/s^2/day in the GoC and Northern Australia, which corresponds with the shown cyclone's track and the most significant pressure and rainfall variations (Deng & Ritchie, 2020). This result is consistent with our along-orbit analysis, where we noted a shift from positive to negative instantaneous LGD variations before and after the cyclone's passage (Figures 7 and 8). In contrast to land hydrology (see Section 4.1.2), this region with a negative trend has lower R^2 values of only 0.6 to 0.75. This indicates that temporal linear regression alone is not sufficient to adequately characterize hydro-meteorological phenomena, but could be improved with a second-order polynomial regression or spline interpolation.

To verify that these signals are related to sub-monthly geophysical phenomena, we compare spatially gridded and Gaussian-filtered post-fit residuals RMS (filtered in the spatial domain using a Gaussian kernel with a radius of 6° and standard deviation $\sigma = 2$) from December 2012 to February 2013 with sub-monthly RMS variations (computed using Equation 15) in the ITSG-Grace2018 daily solutions (Kvas et al., 2019; Mayer-Gürr et al., 2018), resulting in Figure 10.

First, while Figure 10e does not indicate a distinct RMS anomaly at the eastern terminus of Cyclone Oswald's track, Figure 9a reveals a localized negative LGD trend near (26°S, 152°E). This region corresponds to recorded flooding events, and the trend is accompanied by adjusted R^2 values between 0.5 and 0.7. The presence of a measurable trend in the LGD suggests that sub-monthly gravity signals may provide insight into short-term mass redistribution processes associated with extreme weather events. This highlights the potential of LGD-based analyses to complement conventional hydrometeorological data sets for studying cyclone-induced surface mass changes.

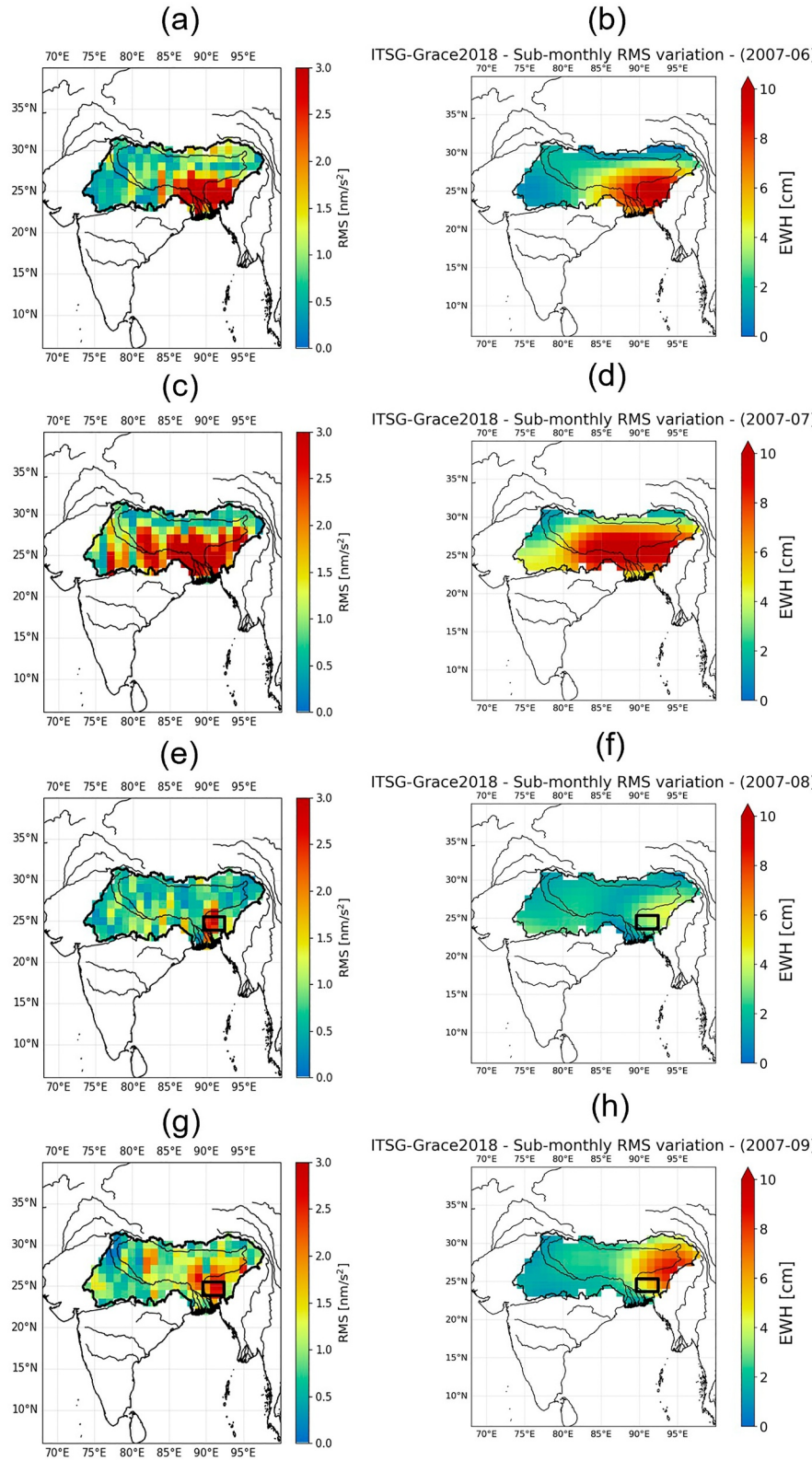

Figure 12. Consecutive monthly grids from June–September 2007 (top to bottom) for the Ganges-Brahmaputra river basin. The left column shows the LGD post-fit residuals root mean square (1° × 1°), and in the right column the sub-monthly variations in equivalent water height in cm of daily Kalman filtered solutions from ITSG-Grace2018.

Secondly, note the range for post-fit residuals was set to 0.5 nm/s^2 to differentiate actual sub-monthly signal from KBR noise (Peidou et al., 2022). We can initially ascertain that January 2013 (Figures 10b and 10e) is notably distinctive, exhibiting significant variations over the entire Northern Australia reaching above 3 nm/s^2 and above 5 cm EWH in post-fit residuals and sub-monthly RMS, respectively. These variations are particularly evident in the GoC, Queensland, and the Northern Territory (or (11°S, 19°S, 132°E, 145°E)) as during January, Australia experienced three major cyclones. In contrast, both daily solutions and post-fit residuals for December 2012 (Figures 10a and 10d), as well as for February 2013 (Figures 10c and 10e), exhibit lower levels of variability within the region with only one cyclone (Christine in December and Rusty in February). This confirms the hypothesis that GRACE detected sub-monthly variabilities attributable to cyclone Oswald, as these regional anomalies align with the cyclone's initial trajectory in the GoC and Queensland.

Furthermore, we observe stronger signals in both the sub-monthly RMS and post-fit residuals along the western coast. These variations (which are considerably less discernible in the post-fit residuals, reaching values of only 1.5 nm/s^2) appear to correlate with the tracks of the severe tropical cyclone Narelle and Peta (see Figure 10e), which occurred between the 5th and 15th, and 22nd and 23rd of January, respectively (BoM). However, although no corresponding signals in the post-fit residuals are detected related to the significant rainfall events on the eastern coast (Figure 10e), the daily solutions seem to capture them (Figure 10b) with an RMS variation of 2.5–3 cm EWH. Interestingly, the effects of cyclones Christine and Rusty are clearly visible in the post-fit residuals (Figures 10d and 10f), but are not discernible in the ITSG daily solutions (Figures 10a and 10c). This discrepancy could be attributed to differences in background modeling used for each data set or the potential exclusion of certain sub-monthly variations in the daily solutions. The fact that post-fit residuals capture these events suggests that they may contain additional geophysical signals not fully represented in the daily solutions.

By demonstrating spatial and temporal correlations between both methods, particularly in Northern Australia, where Cyclone Oswald originated, we confirm that post-fit residuals encompass high-frequency geophysical signals induced by hydro-meteorological phenomena. Additionally, our analysis extended to the severe cyclones in February–March 2007 (cyclones George, Jacob and Kara) revealing significant LGD variations—most notably for Cyclone George—which correlated with each cyclone's trajectory (see Figures S6 in Supporting Information S1).

4.3.3. Point-Mass Model Analysis

As a final step, we investigate whether these anomalies can directly be attributed to the moving cyclonic system. We assume the cyclone to be a point mass which tries to account for the unmodelled (AOD1B) cyclonic traces in post-fit residuals. We set this mass to be constant and equal to 30 Gt, which is a first-order estimation using spatially integrated weekly precipitation data provided by the BoM, for the week of 19–25 of January (for more details see Figure S5 in Supporting Information S1). This mass also coincides with the integrated mass anomaly considering the cyclone's highest pressure difference variations of approx. 10–15 hPa and a radius of 500 km (Deng & Ritchie, 2020). We limit the analysis to a case in which we see agreement between the model and post-fit residuals in Figure 11a, and one case where there is no alignment in Figure 11b.

In Figure 11a, one can see that the anomaly is first highly localized as seen from the ascending track with an LGD of −5 nm/s^2, and after half a day, the anomaly spreads leading to a wider LGD anomaly with slightly smaller magnitude of −4 nm/s^2 in the descending track. This descending track corresponds to arc 4d in Figure 8, which passes over the northern region of Queensland at the same latitudes as the GoC. In this aligned scenario, the location and timing of both anomalies appear to correlate with the cyclone's path. This suggests that the observed signal is likely tied to the cyclone's highest central pressure drop from 996 to 990–991 hPa, which occurred between the 21st and 22nd of January (Deng & Ritchie, 2020). Furthermore, we can discern information regarding the anomalies' spatial distribution by observing the changes in the width of the LGD peak (Spero, 2021). The width of the anomaly matches a point-like mass (below 300 km) change in the earlier ascending track, whereas, after half a day, the width has increased and no longer matches with the point-mass model suggesting a significant spatial spread (larger than 400 km as described by Spero (2021)).

Figure 11b demonstrates that there is no alignment observed in both the ascending and descending tracks (with the latter corresponding to arc 8d in Figure 8). This results in a potential phase delay of 5 min, accompanied by post-fit

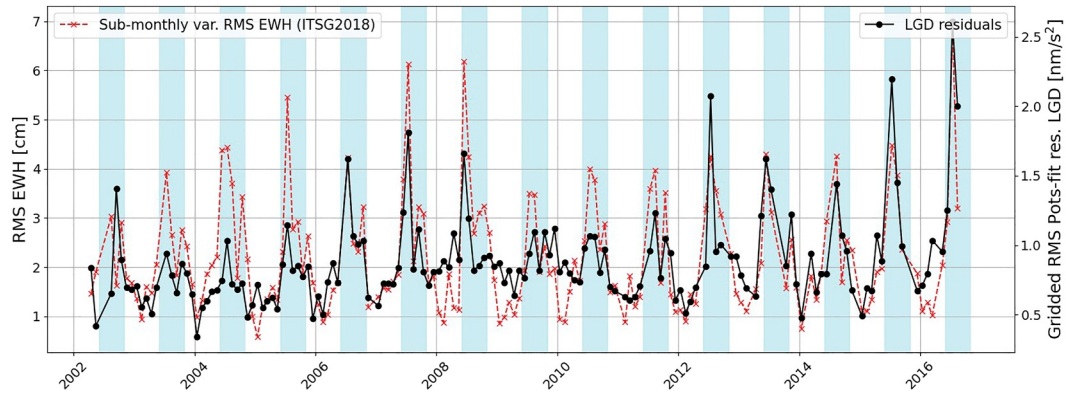

Figure 13. Time series of gridded root mean square (RMS) LGD post-fit residuals, and RMS variability w.r.t. Monthly mean of ITSG daily solutions in the Ganges-Brahmaputra basin from April 2002 to August 2016. Shaded regions depict monsoon seasons from June to mid-October.

residual anomalies at −15° latitude. The lack of alignment suggests that the observed post-fit residuals cannot be adequately explained by the simple 30 Gt point-mass model, and thus we cannot confirm if they are caused by the moving cyclonic system. This is most likely due to the fact that on the 27th–28th of January, the cyclone started dissipating (Bureau of Meteorology, 2013), and thus the pressure anomaly started decreasing slowly again (Deng & Ritchie, 2020; Leroux et al., 2019).

It is important to highlight that the majority of cases we examined (not shown) displayed only partial or no alignment between the 30 Gt point-mass cyclone model and the post-fit residuals. When we refer to partial alignment, we identify two main issues. First, there might be a phase delay in which the point-mass model does not match the timing of the post-fit residuals, especially on land. This suggest the hypothesis that LGDs are not particularly sensitive to pressure variations given their wide spatial footprint; only when precipitation collects on fairly restricted areas on land, are then these data sensitive to the effects of cyclones. The second issue involves the magnitude of the LGD not aligning with the point mass model. This misalignment suggests problems with the assumption of constant (point) mass, stemming from variations in precipitation and pressure along the cyclone's landfall. This is consistent with the fact that as the cyclone moved inland, its pressure difference decreased from its maximum of 15 hPa (January 22nd) to approx. 2 hPa (from January 28th) (Leroux et al., 2019). The latter issue could also be attributed to the absence of an observed intersection between the GRACE and cyclone ground tracks. As GRACE is not in proximity to the cyclone's path, the presence of unrelated mass anomalies could superimpose with the cyclone's (un)modeled signal leading to the observed lack of alignment.

The findings highlight that there is strong evidence supporting a connection between the cyclone's path and the observed anomaly in the aligned scenario. This is particularly evident in the tracks from January 21st and 22nd, where the observed anomalies strongly correlate with the cyclone's movement, timing, and highest pressure variations (Figure 11a). The significant magnitude of these anomalies, which are absent in monthly gravity field models, suggests that the cyclone's central pressure drop (when sufficiently intense) and rainfall mass redistribution are likely the primary drivers. However, the majority of cases display partial or no alignment, highlighting the limitations of the simple 30 Gt point-mass model in capturing the complexities of the observed signal.

4.4. Land Hydrology High-Frequency Mass Change Signals

The Ganges-Brahmaputra river basin is renowned for its significant hydrological variations, primarily due to the rainy season coinciding with the summer monsoon, which typically commences in June and concludes in mid-October. From June–September 2007, Bangladesh experienced severe flooding, impacting 42% of the country (Islam et al., 2010), due to the increased melting of the Himalayan glaciers.

As performed in the previous section, we compare LGD post-fit residuals to the sub-monthly RMS variations (Equation 15) in the ITSG-Grace2018 daily solutions as can be seen in Figure 12. We confirm the findings from

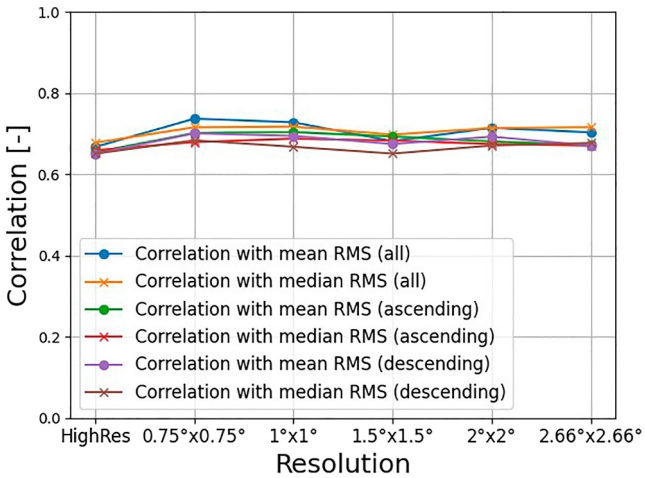

Figure 14. Sensitivity analysis of the correlation coefficient between the root mean square of post-fit residuals and the sub-monthly variability in ITSG daily solutions, as influenced by spatial resolution, ground-track type, and statistical estimator. The term "HighRes" denotes the case in which the post-fit residuals were not spatially gridded.

previous research (Gouweleeuw et al., 2018), which indicated that these daily Kalman-filtered solutions exhibit sub-monthly variability due to the abrupt flooding events from June to September, as shown in Figure 12 (left column). Notably, for June and July (Figures 12a–12d), sub-monthly variabilities reach values of 10 cm in EWH coinciding both with LGD variations and the known regions of significant rainfall from 500 to even 1,000 mm (refer to Figure 4 by Islam et al. (2010)). The opposite is true for August (Figures 12e and 12f), where both the rainfall and these variabilities reach a minimum, suggesting that monthly models adequately represent the overall water storage fluctuations in the region, as also evidenced by the lower observed RMS in the post-fit residuals.

Furthermore, we observe significant spatial correlations with Pearson correlation coefficients of 0.81 and 0.78 between the LGD post-fit residuals and the sub-monthly RMS variabilities in the daily solutions for June and July, whereas, for August and September, these are 0.38 and 0.56, respectively. As performed in Section 4.3, to make this analysis more comparable between both variables, we apply a 2D Gaussian filter (with a radius of 6 deg at $\sigma = 2$ to match the smoothing applied on the gridded daily solutions) to the post-fit residuals grid. Using this method, the spatial correlations increase to 0.92 and 0.95 for June and July, and 0.62 and 0.82 for August and September, confirming a better match with the daily solutions' spatial resolution. We refer the reader to Figure S7 in Supporting Information S1 to show the effect of the standard deviation parameter σ on the smoothing process. By utilizing the L1B 5s sampling rate, we better localize the two flood peaks in August and September in the smaller Meghna River, centered at (24°N, 91°E) (Islam et al., 2010), highlighted in Figures 12e and 12f, whereas the daily solutions have a limited spatial resolution (Gouweleeuw et al., 2018). This is further confirmed by analyzing the instantaneous or along-orbit post-fit residuals, which show localized variations near the flooded region in both the ascending and descending tracks (see Figures S8 and S9 in Supporting Information S1). Finally, a longitudinal phase shift of 1–4° is evident between the spatial variations in post-fit residuals and the daily solutions, which we speculate is attributed to the incorporated hydrological model statistics in the Kalman filtering constraints and pre-applied spatial smoothing of the daily solutions.

After examining these single flooding events, we conduct the same aggregate statistical analysis described in Section 4.2. This analysis is applied to both the gridded LGD residuals (solid line) and the daily solutions' variability (dashed line), resulting in Figure 13.

Two key observations can be made. First, there is significant sub-monthly variability in both post-fit residuals and daily solutions during the monsoon seasons, which are indicated by the shaded areas. Second, a high correlation of 0.73 exists between these two time-series, confirming that post-fit residuals effectively reflect sub-monthly variabilities and that these are a consistent seasonal phenomenon that must be accounted for in regional mass change models.

Furthermore, we performed a sensitivity analysis to assess the robustness of our results. This involved varying the spatial resolution of the gridded LGDs, separating the ground tracks into ascending and descending categories, and using either the mean or median as statistical estimators, as illustrated in Figure 14. We found that changes in spatial resolution resulted in relatively insignificant alterations in correlation. However, separating the data by ground-track type and using different statistical estimators led to small correlation changes ranging from −0.09 to 0.02. Additionally, we truncated the GRACE mission data from July 2003 to eliminate potential issues related to the one SCA phase. This adjustment yielded a slight increase in correlation coefficients of approximately 0.025. Overall, these changes remain relatively minor, confirming that the observed correlation is not coincidental but rather a robust feature of the data set. The consistency of results across different grid resolutions and statistical approaches reinforces the reliability of post-fit residuals in capturing sub-monthly mass variations. This strengthens confidence in their use as an independent data set for validating regional mass change models and studying high-frequency geophysical processes.

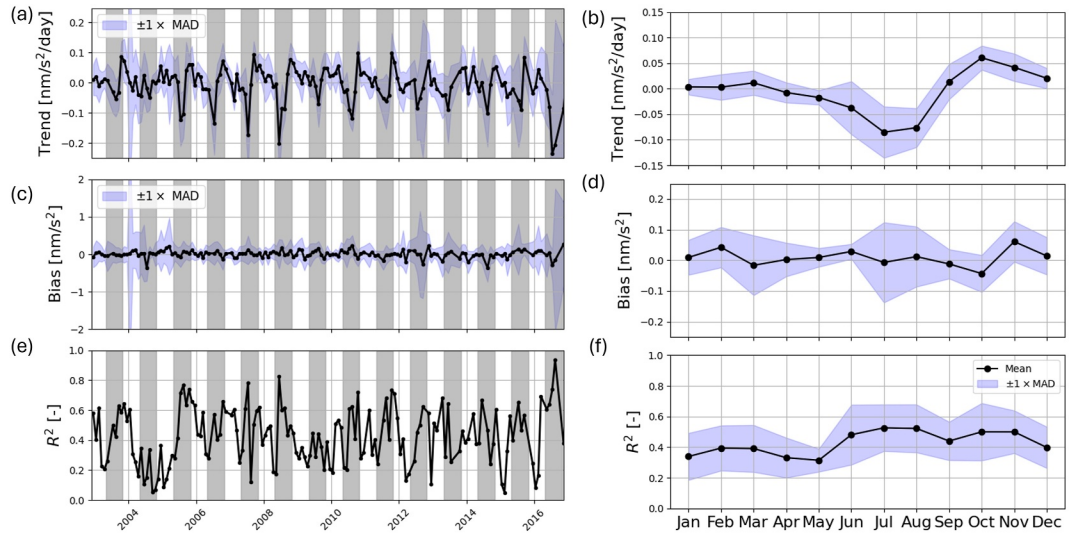

Figure 15. The left column shows the time series of gridded linear regression variables such as trend (a), bias (c) and R^2 (e) related to LGD post-fit residuals for the entire Ganges-Brahmaputra river basin. Shaded regions depict monsoon seasons from June to mid-October. The right column shows the average characteristic per month for the trend (b), bias (d) and R^2 (f).

Finally, we present the results of the complete time series of sub-monthly LGD linear regression characteristics (trend, bias, and R^2) using the methodology presented in Section 3 in Figure 15 to characterize the periodic nature of the sub-monthly signals. We can observe a seasonal pattern in the trend signal (Figure 15a). This pattern is characterized by a sharp transition from negative values during June to August, to positive values in September and October (Figure 15b). The monsoon flood events of 2007 exhibit one of the most significant trend changes, alongside those in 2006, 2008, and 2016, with a shift from −0.17 to 0.1 nm/s^2/day. This change corresponds with the increased hydrological activity (i.e., rainfall and flooding) noted during these events (Islam et al., 2010). Additionally, the adjusted R^2 values show substantial peaks, reaching between 0.6 and 0.95 (Figure 15e), with an average monthly maximum of 0.56 observed during the monsoon seasons (Figure 15f). Lastly, as discussed in Section 4.1.2, the mid-month bias does not display any discernible temporal pattern (with a slight increase in MAD spread during July), as evidenced by Figures 15c and 15d. This lack of a temporal pattern in the bias further supports the conclusion that CSR's models accurately capture the monthly average without leaving any residual bias in the post-fit residuals.

These results therefore affirm that the L1B post-fit residuals indeed capture significant seasonal signals associated with sub-monthly land hydrology which can be well described by a spatial-temporal linear regression. Furthermore, the fact that these seasonal variations can be described by a spatial-temporal linear regression provides valuable insights into how land hydrological signals, such as those associated with monsoon flooding, evolve over time and space. This approach not only helps in understanding the dynamics of land hydrology at a finer temporal scale but also enables improved predictions of future hydrological events and contributes to refining models of water storage changes.

4.5. Global Temporal Correlations Between Post-Fit Residuals and ITSG Daily Solutions

We now provide a global overview of the spatial distribution of the temporal correlations between the monthly gridded RMS of post-fit residuals (e.g., Figures 1f or 2f) and the sub-monthly variability of daily solutions, as illustrated in Figure 16. This analysis is crucial as it provides insights into the spatial distribution of temporal correlations, which helps assess the accuracy and consistency of the geophysical models derived from GRACE data. By focusing on sub-monthly variability, we can refine our understanding of hydrological and glaciological processes that operate on timescales shorter than a month, which may be masked when using monthly correlations. Furthermore, we chose this approach because at least a month's worth of data is required to ensure sufficient global coverage, filling all grid cells for a comprehensive analysis.

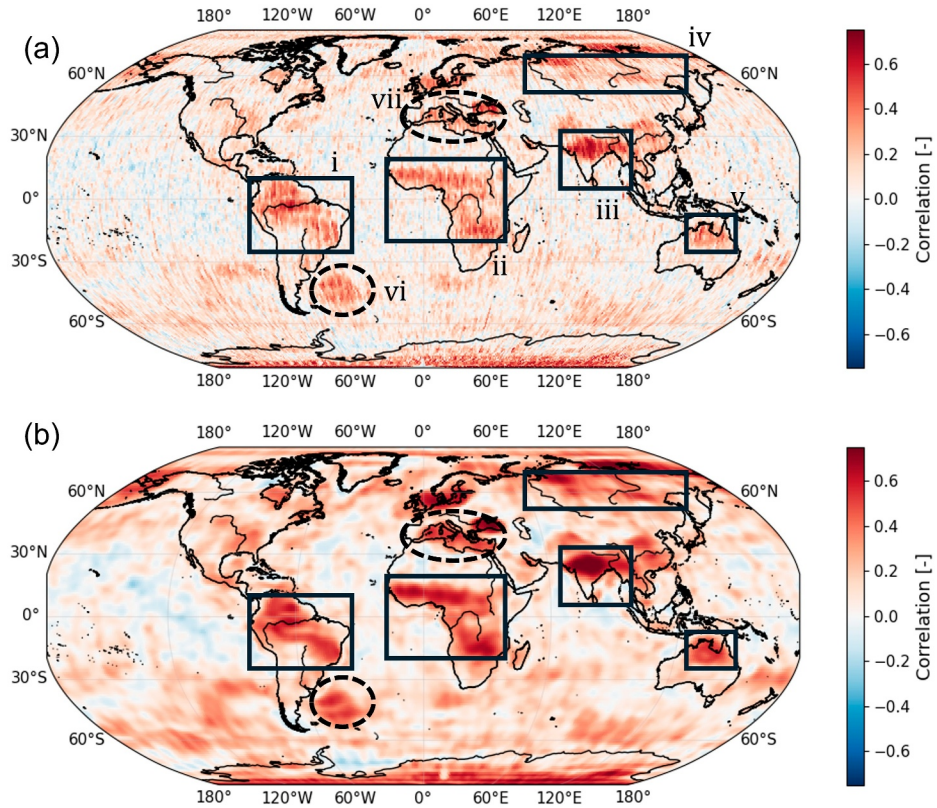

Figure 16. Global overview of the spatial distribution of temporal correlations between post-fit residuals as LGDs (1° × 1°) and root mean square sub-monthly variability of ITSG-Grace2018 daily solutions (from July 2003 to August 2016). The temporal correlations are shown without (a) and with (b) applied Gaussian spatial smoothing (radius of 6 deg and $\sigma = 2$) on the post-fit residuals grids.

As anticipated, applying Gaussian spatial smoothing (radius of 6 deg at $\sigma = 2$) on the post-fit residuals grids increases the temporal correlations by 0.1–0.2 both locally and globally (as seen in Figure 16 from sub-figure a to b). This is especially evident in major river basins (i to iv) and south-eastern oceanic regions (most significantly found in vi). This improvement occurs because we better align with the original spatial resolution of the daily solutions, which is approximately 500 km.

We observe significant correlations (above 0.5) in several major river basins. In South America (see highlight *i* in Figure 16), the Amazon, Orinoco, and La Plata river basins showed correlations between 0.5 and 0.6. In Central Africa (ii), notable correlations (up to 0.65) were found in the Chad, Nile, and Congo river basins. In Asia (iii), the Ganges-Brahmaputra and Indus River basins also demonstrated strong correlations. In Northern Australia (v), we identified correlations reaching up to 0.6 related to the aforementioned hydro-meteorological sub-monthly variations due to cyclonic activity. Of all river basins, the Indus and Ganges-Brahmaputra basins exhibited the highest temporal correlations, with values ranging from 0.60 to as high as 0.75.

Temporal correlations are not limited to land hydrology sub-monthly signals; they can also be seen in the Argentine ocean basin (vi), the Mediterranean (vii), and the North Sea, as well as along the western coast of Canada and Alaska, and the northern coast of Russia (iv). The most noticeable oceanic correlations are within the Argentine basin which are related to the high-frequency component of the rotating dipole mode around the Zapiola rise. Sub-monthly glaciology signals predominantly appear in Antarctica, with a limited presence in Greenland (with correlations capped at 0.4).

Lastly, we can identify several regions with no significant temporal correlations, primarily in the oceans, which we speculate may be related to remaining KBR noise in the post-fit residuals that dominate compared to the geophysical signal. Given the high correlations between post-fit residuals and daily solutions in the highly active

hydrological river basins, this approach further validates the assumed geophysical constraints implemented within the ITSG-Grace2018 daily models.

5. Conclusions

In this study, we examined the use of K-band range-rate post-fit residuals from the GRACE mission provided by CSR, which were transformed into Line-of-Sight Gravity Differences (LGD), to identify and characterize high-frequency mass change signals. The purpose of this is to answer:

> *How can high-frequency geophysical signals within GRACE Level-1B post-fit residuals be identified, characterized, and validated using spatial correlation analysis and comparisons with daily gravity field solutions?*

Our findings confirmed previous observations related to the geophysical frequency range of [0.9, 11] mHz of sub-monthly signals in post-fit residuals while significantly advancing the understanding of these residuals by providing detailed geophysical attribution using a spatial-temporal linear regression and Root-Mean Squared characterization and validation of their sub-monthly nature.

We focused on three main categories of high-frequency signals: oceanic, meteorological, and hydrological processes. In the Zapiola region, we detected significant high-frequency oceanic mass change signals potentially linked to the dynamics of a rotating dipole-like mode. However, a comparison of SLA and LGD variations through statistical analysis showed no strong correlations (below 0.25), suggesting that further research is needed.

During Cyclone Oswald, we identified significant meteo-hydrological signals in the GoC, supporting earlier research that linked LGD anomalies to rapid pressure changes in this region. Our extended analysis further revealed that the areas of LGD anomalies aligned closely with the cyclone's path and associated precipitation patterns. For the first time, we validated the sub-monthly nature of these anomalies using RMS variations from ITSG-Grace2018 daily solutions. The spatial correlations between the LGD anomalies and these daily solutions reinforced the interpretation of sub-monthly variability. Additionally, we developed a preliminary proto-mass change model that approximates the cyclone as a point mass, which effectively localized two cyclonic sub-monthly signals during one of the cyclone's peak intensities over the GoC. However, limitations in this simplified model became evident as the majority of cases have partial to no alignment with post-fit residuals, highlighting the necessity of a more advanced mass change modeling framework.

Lastly, we also analyzed LGD residuals in the Ganges-Brahmaputra river basin during the 2007 monsoon season and we showed that regions of significant LGD residuals variations correlated with sub-monthly variations in the ITSG-Grace2018 daily solutions. We extended this analysis from July 2003 to August 2016 and demonstrated first that there is a significant correlation of 0.67–0.74 between these two time-series and secondly, that sub-monthly variabilities both in LGD residuals and daily solutions tend to peak during monsoon seasons. Additionally, the 5-s sampling rate of the Level-1B data enabled us to potentially better localize critical flooding peaks in the Meghna river, which was not achievable with the coarse spatial resolution of the daily solutions.

This study provides the first extensive geophysical characterization of high-frequency signals within GRACE post-fit residuals—specifically, those from the widely used CSR RL06 Level-2 data product. Previous work primarily suggested that post-fit residuals contained sub-monthly signals but lacked systematic attribution to specific geophysical processes or robust validation methods. Here, we introduced spatial plots of statistics and linear regression parameters, and we performed a cross-validation using the ISTG-Grace2018 daily solutions for the first time to demonstrate their sub-monthly nature. This highlights the broader potential of these residuals to offer improved temporal and spatial resolution for studying rapid changes in Earth's gravity field.

Overall, our findings underscore the value of GRACE post-fit residuals as a valuable product, with the potential to enhance the temporal and spatial resolution of gravity-based mass change monitoring. Future research will focus on leveraging these residuals to develop a framework for high-frequency mass change modeling.

Conflict of Interest

The authors declare no conflicts of interest relevant to this study.

Data Availability Statement

GRACE Level-1B data used in this study are available at (NASA Jet Propulsion Laboratory (JPL), 2018; Case et al., 2010b). Specifications related to CSR's Level-2 processing are documented in (S. V. Bettadpur, 2018). CSR post-fit data are available at https://doi.org/10.18738/T8/VY3U8L (S. Bettadpur et al., 2025). Level-4 altimetry data are available at (CMEMS, 2021). The gridded ITSG-Grace2018 daily solutions can be found in (Mayer-Gürr et al., 2018). Other data sets used in this study include Oswald cyclone tracking and rainfall data from the Australian BoM (BoM, 2024c). Precipitation grids are described in (BoM, 2024a), and cyclone track data are described in (BoM, 2024b).

Acknowledgments
We thank Prof. Byron Tapley, Himanshu Save, Srinivas V. Bettadpur and the Center for Space Research, CSR, for providing us with their residual RL06 Level-1B range-rate data.

References

Allgeyer, S., Tregoning, P., McQueen, H., McClusky, S. C., Potter, E. K., Pfeffer, J., et al. (2022). ANU GRACE data analysis: Orbit modeling, regularization and inter-satellite range acceleration observations. *Journal of Geophysical Research: Solid Earth*, *127*(2), e2021JB022489. https://doi.org/10.1029/2021JB022489

Bandikova, T., Flury, J., & Ko, U.-D. (2012). Characteristics and accuracies of the GRACE inter-satellite pointing. *Advances in Space Research*, *50*(1), 123–135. https://doi.org/10.1016/j.asr.2012.03.011

Bandikova, T., McCullough, C., Kruizinga, G. L., Save, H., & Christophe, B. (2019). GRACE accelerometer data transplant. *Advances in Space Research*, *64*(3), 623–644. https://doi.org/10.1016/j.asr.2019.05.021

Bettadpur, S., Save, H., Tapley, B., Nagel, P., Kang, Z., Poole, S., et al. (2025). CSR RL06 GRACE geofit and postfit dataset. *Texas Data Repository*. https://doi.org/10.18738/T8/VY3U8L

Bettadpur, S. V. (2018). GRACE Level-2 processing standards document. *Computer software manual*. Retrieved from https://podaac-tools.jpl.nasa.gov/drive/files/allData/grace/docs/L2-CSR006_ProcStd_v5.0.pdf

BoM, A. (2024a). Australian climate maps – Rainfall [Dataset]. Retrieved from https://reg.bom.gov.au/climate/maps/rainfall/

BoM, A. (2024b). Database of past tropical cyclone tracks [Dataset]. Retrieved from http://www.bom.gov.au/cyclone/history/index.shtml

BoM, A. (2024c). Oswald cyclone tracking and rainfall data [Dataset]. *Retrieved from*. http://www.bom.gov.au/

Bonin, J. A., & Save, H. (2020). Evaluation of sub-monthly oceanographic signal in GRACE "daily" swath series using altimetry. *Ocean Science*, *16*(2), 423–434. https://doi.org/10.5194/os-16-423-2020

Bureau of Meteorology. (2013). Tropical cyclone oswald. Retrieved from http://www.bom.gov.au/cyclone/history/Oswald.shtml

Case, K., Kruizinga, G., & Wu, S. (2010a). GRACE level 1B data product user handbook. *Computer software manual*. Retrieved from https://podaac-tools.jpl.nasa.gov/drive/files/allData/grace/docs/Handbook_1B_v1.3.pdf(JPLPublicationD-22027

Case, K., Kruizinga, G., & Wu, S.-C. (2010b). Grace level 1b data product user handbook.

CMEMS. (2021). Global ocean along-track delayed-mode sea level [Dataset]. *CMEMS*. https://doi.org/10.48670/moi-00148

Croteau, M. J., Nerem, R. S., Loomis, B. D., & Sabaka, T. J. (2020). Development of a daily grace mascon solution for terrestrial water storage. *Journal of Geophysical Research: Solid Earth*, *125*(3), e2019JB018468. https://doi.org/10.1029/2019JB018468

de Miranda, A. P., Barnier, B., & Dewar, W. K. (1999). On the dynamics of the zapiola anticyclone. *Journal of Geophysical Research*, *104*(C9), 21137–21149. https://doi.org/10.1029/1999JC900042

Deng, D., & Ritchie, E. A. (2020). Rainfall mechanisms for one of the wettest tropical cyclones on record in Australia—Oswald (2013). *Monthly Weather Review*, *148*(6), 2503–2525. https://doi.org/10.1175/MWR-D-19-0168.1

Eicker, A., Jensen, L., Wöhnke, V., Dobslaw, H., Kvas, A., Mayer-Gürr, T., & Dill, R. (2020). Daily GRACE satellite data evaluate short-term hydro-meteorological fluxes from global atmospheric reanalyses. *Scientific Reports*, *10*(1), 4504. https://doi.org/10.1038/s41598-020-61166-0

Flechtner, F. (2007). *Gravity recovery and climate experiment AOD1B product description document for product releases 01 to 04 (technical report)*. GeoForschungszentrum Potsdam. (Available from GFZ Potsdam).

Flechtner, F., Dahle, C., Neumayer, K. H., König, R., & Förste, C. (2010). The release 04 CHAMP and GRACE EIGEN gravity field models. In F. M. Flechtner, T. Gruber, A. Güntner, M. Mandea, M. Rothacher, T. Schöne, & J. Wickert (Eds.), *System Earth via geodetic-geophysical space techniques* (pp. 41–58). Springer Berlin Heidelberg. https://doi.org/10.1007/978-3-642-10228-8_4

Ghobadi-Far, K., Han, S. C., Allgeyer, S., Tregoning, P., Sauber, J., Behzadpour, S., et al. (2020). GRACE gravitational measurements of tsunamis after the 2004, 2010, and 2011 great earthquakes. *Journal of Geodesy*, *94*(7), 1–9. https://doi.org/10.1007/S00190-020-01395-3

Ghobadi-Far, K., Han, S. C., Loomis, B. D., & Luthcke, S. B. (2019). *On computation of potential, gravity and gravity gradient from GRACE inter-satellite ranging data: A systematic study* (Vol. 149, pp. 91–96). International Association of Geodesy Symposia. https://doi.org/10.1007/1345_2018_39

Ghobadi-Far, K., Han, S. C., McCullough, C. M., Wiese, D. N., Ray, R. D., Sauber, J., et al. (2022). Along-orbit analysis of GRACE Follow-On inter-satellite laser ranging measurements for sub-monthly surface mass variations. *Journal of Geophysical Research: Solid Earth*, *127*(2), e2021JB022983. https://doi.org/10.1029/2021JB022983

Ghobadi-Far, K., Han, S.-C., Weller, S., Loomis, B. D., Luthcke, S. B., Mayer-Gürr, T., & Behzadpour, S. (2018). A transfer function between line-of-sight gravity difference and GRACE intersatellite ranging data and an application to hydrological surface mass variation. *Journal of Geophysical Research: Solid Earth*, *123*(10), 9186–9201. https://doi.org/10.1029/2018JB016088

Goswami, S. (2018). Understanding the sensor noise in the GRACE range-rate observations by analyzing their residuals (doctoral dissertation, DGK). Retrieved from http://www.dgk.badw.de

Gouweleeuw, B. T., Kvas, A., Gruber, C., Gain, A. K., Mayer-Gürr, T., Flechtner, F., & Güntner, A. (2018). Daily GRACE gravity field solutions track major flood events in the ganges–Brahmaputra Delta. *Hydrology and Earth System Sciences*, *22*(5), 2867–2880. https://doi.org/10.5194/hess-22-2867-2018

Han, S.-C., Ghobadi-Far, K., Yeo, I.-Y., McCullough, C. M., Lee, E., & Sauber, J. (2021a). GRACE Follow-On revealed Bangladesh was flooded early in the 2020 monsoon season due to premature soil saturation. *Proceedings of the National Academy of Sciences*, *118*(47), e2109086118. https://doi.org/10.1073/pnas.2109086118

Han, S.-C., Ray, R., & Hughes, C. (2014). High-frequency (20–60 days) ocean mass variation over the Argentine basin observed from GRACE. In *Proceedings of the grace science team meeting*. Retrieved from https://www.gfz-potsdam.de/en/section/global-geomonitoring-and-gravity-field/projects/gravity-recovery-and-climate-experiment-follow-on-grace-fo-mission/gstm/gstm-2014/

Han, S.-C., Sauber, J., & Luthcke, S. (2010). Regional gravity decrease after the 2010 Maule (Chile) earthquake indicates large-scale mass redistribution. *Geophysical Research Letters*, *37*(23), L23307. https://doi.org/10.1029/2010GL045449

Han, S.-C., Yeo, I.-Y., Khaki, M., McCullough, C. M., Lee, E., & Sauber, J. (2021b). Novel along-track processing of GRACE Follow-On laser ranging measurements found abrupt water storage increase and land subsidence during the 2021 march Australian flooding. *Earth and Space Science*, *8*(11), e2021EA001941. https://doi.org/10.1029/2021EA001941

Hughes, C. W., Stepanov, V. N., Fu, L.-L., Barnier, B., & Hargreaves, G. W. (2007). Three forms of variability in Argentine basin ocean bottom pressure. *Journal of Geophysical Research*, *112*(C1), C01011. https://doi.org/10.1029/2006JC003679

Islam, A. S., Haque, A., & Bala, S. K. (2010). Hydrologic characteristics of floods in Ganges–Brahmaputra–Meghna (GBM) Delta. *Natural Hazards*, *54*(3), 797–811. https://doi.org/10.1007/s11069-010-9504-y

Khan, I. R., & Ohba, R. (1999). 7). Closed-form expressions for the finite difference approximations of first and higher derivatives based on Taylor series. *Journal of Computational and Applied Mathematics*, *107*(2), 179–193. https://doi.org/10.1016/S0377-0427(99)00088-6

Killett, B., Wahr, J., Desai, S., Yuan, D., & Watkins, M. (2011). Arctic Ocean tides from GRACE satellite accelerations. *Journal of Geophysical Research*, *116*(C11), 11005. https://doi.org/10.1029/2011JC007111

Kurtenbach, E., Eicker, A., Mayer-Gürr, T., Holschneider, M., Hayn, M., Fuhrmann, M., & Kusche, J. (2012). Improved daily GRACE gravity field solutions using a kalman smoother. *Journal of Geodynamics*, *59–60*, 39–48. https://doi.org/10.1016/j.jog.2012.02.006

Kvas, A., Behzadpour, S., Ellmer, M., Klinger, B., Strasser, S., Zehentner, N., & Mayer-Gürr, T. (2019). ITSG-Grace2018: Overview and evaluation of a new GRACE-Only gravity field time series. *Journal of Geophysical Research: Solid Earth*, *124*(8), 9332–9344. https://doi.org/10.1029/2019JB017415

Lemoine, J.-M., & Bourgogne, S. (2020). RL05 monthly and 10-day gravity field solutions from CNES/GRGS. In *Gstm2020-51*. https://doi.org/10.5194/gstm2020-51

Lemoine, J.-M., Bruinsma, S., Loyer, S., Biancale, R., Marty, J.-C., Perosanz, F., & Balmino, G. (2007). Temporal gravity field models inferred from GRACE data. *Advances in Space Research*, *39*(10), 1620–1629. https://doi.org/10.1016/j.asr.2007.03.062

Leroux, M.-D., Nguyen-Hankinson, M. C., Davidson, N. E., Callaghan, J., Tory, K., Wain, A., & Huang, X. (2019). Environmental interactions during the extreme rain event associated with ex-tropical cyclone Oswald (2013). *Journal of Southern Hemisphere Earth Systems Science*, *69*(1), 2–16. https://doi.org/10.1071/ES19016

Mayer-Gürr, T., Behzadpur, S., Ellmer, M., Kvas, A., Klinger, B., Strasser, S., & Zehentner, N. (2018). ITSG-Grace2018–Monthly, daily and static gravity field solutions from GRACE [Dataset]. https://doi.org/10.5880/ICGEM.2018.003

NASA Jet Propulsion Laboratory (JPL). (2018). Grace level 1b jpl release 3.0. *NASA Physical Oceanography Distributed Active Archive Center*. https://doi.org/10.5067/GRJPL-L1B03

Peidou, A., Landerer, F., Wiese, D., Ellmer, M., Fahnestock, E., McCullough, C., et al. (2022). Spatiotemporal characterization of geophysical signal detection capabilities of GRACE-FO. *Geophysical Research Letters*, *49*(1), e2021GL095157. https://doi.org/10.1029/2021GL095157

Pini, A. J. (2012). *Investigation of the effect of repeat orbits on GRACE gravity recovery (unpublished master's thesis)*. University of Texas-Austin.

Ramillien, G., Seoane, L., Schumacher, M., Forootan, E., Frappart, F., & Darrozes, J. (2020). Recovery of rapid water mass changes (RWMC) by kalman filtering of GRACE observations. *Remote Sensing*, *12*(8), 1299. https://doi.org/10.3390/rs12081299

Rateb, A., Save, H., Sun, A. Y., & Scanlon, B. R. (2024). Rapid mapping of global flood precursors and impacts using novel five-day GRACE solutions. *Scientific Reports*, *14*(1), 13841. https://doi.org/10.1038/s41598-024-64491-w

Schindelegger, M., Harker, A. A., Ponte, R. M., Dobslaw, H., & Salstein, D. A. (2021). Convergence of daily GRACE solutions and models of submonthly ocean bottom pressure variability. *Journal of Geophysical Research: Oceans*, *126*(2), e2020JC017031. https://doi.org/10.1029/2020JC017031

Schmidt, R., Flechtner, F., Meyer, U., Neumayer, K.-H., Dahle, C., König, R., & Kusche, J. (2008). Hydrological signals observed by the GRACE satellites. *Surveys in Geophysics*, *29*(4–5), 319–334. https://doi.org/10.1007/s10712-008-9033-3

Spero, R. (2021). Point-mass sensitivity of gravimetric satellites. *Advances in Space Research*, *67*(5), 1656–1664. https://doi.org/10.1016/j.asr.2020.12.019

Sun, A. Y., Save, H., Rateb, A., Jiang, P., & Scanlon, B. R. (2024). Deciphering the role of total water storage anomalies in mediating regional flooding. *Geophysical Research Letters*, *51*(16), e2023GL108126. https://doi.org/10.1029/2023GL108126

Tregoning, P., Lambeck, K., & Ramillien, G. (2008). GRACE estimates of sea surface height anomalies in the gulf of Carpentaria, Australia. *Earth and Planetary Science Letters*, *271*(1), 241–244. https://doi.org/10.1016/j.epsl.2008.04.018

Volkov, D. L., & Fu, L.-L. (2008). The role of vorticity fluxes in the dynamics of the zapiola anticyclone. *Journal of Geophysical Research*, *113*(C11), C11015. https://doi.org/10.1029/2008JC004841

Wahr, J. (2015). In *Time-variable gravity from satellites*. Elsevier (pp. 193–213). https://doi.org/10.1016/B978-0-444-53802-4.00065-8

Weigelt, M. (2017). The acceleration approach. In M. Naeimi & J. Flury (Eds.), *Global gravity field modeling from satellite-to-satellite tracking data, lecture notes in Earth system Sciences* (pp. 127–160). Springer International Publishing.

Wouters, B., Gardner, A. S., & Moholdt, G. (2019). Global glacier mass loss during the GRACE satellite mission (2002-2016). *Frontiers in Earth Science*, *7*, 96. https://doi.org/10.3389/feart.2019.00096

Xiong, Y., Feng, W., Zhou, X., Kusche, J., Shen, Y., Yang, M., et al. (2024). 09). Separation of earthquake and hydrology signals from GRACE satellites data via independent component analysis: A case study in the Sumatra region. *Geophysical Journal International*, *239*(3), 1597–1616. https://doi.org/10.1093/gji/ggae351

Yu, Y., Chao, B. F., García-García, D., & Luo, Z. (2018). Variations of the Argentine Gyre observed in the GRACE time-variable gravity and ocean altimetry measurements. *Journal of Geophysical Research: Oceans*, *123*(8), 5375–5387. https://doi.org/10.1029/2018JC014189